Jovian Auroral Ion Precipitation: X-Ray Production from Oxygen and Sulfur Precipitation

S. J. Houston[1,2], T. E. Cravens[1], D. R. Schultz[3,4], H. Gharibnejad[3,5], W. R. Dunn[6,7,8], D. K. Haggerty[9], A. M. Rymer[9], B. H. Mauk[9], N. Ozak[10]

[1]Department of Physics and Astronomy, University of Kansas, Lawrence, KS, USA
[2]Now at The Johns Hopkins University Applied Physics Laboratory, Laurel, Maryland, USA
[3]Department of Physics, University of North Texas, Denton, TX, USA
[4]Now at Department of Physics and Astronomy, Northern Arizona University, Flagstaff, AZ, USA
[5]Now at National Institute of Standards and Technology, Gaithersburg, MD, USA
[6]Mullard Space Science Laboratory, University College London, London, UK
[7]University College London Center for Planetary Science, London, UK
[8]Harvard-Smithsonian Center for Astrophysics, Cambridge, MA, USA
[9]The Johns Hopkins University Applied Physics Laboratory, Laurel, Maryland, USA
[10]CluePoint S.A., Axis Parc, Rue Emile Francqui 1, 1435 Mont-Saint-Guibert, Belgium, EU

Key Points:

- Heavy ion precipitation into the Jovian atmosphere can produce the observed auroral X-ray emission.
- Using Juno measurements of ion fluxes over Jupiter's pole we simulate X-ray spectra.
- We compare our approximated synthetic X-ray spectra produced by *in situ* data to observed emission.

Corresponding author: T. E. Cravens, `cravens@ku.edu`

Abstract

Many attempts have been made to model X-ray emission from both bremsstrahlung and ion precipitation into [c1]Jupiter's polar caps. Electron bremsstrahlung modeling has fallen short of producing the total overall power output observed by earth-orbit-based X-ray observatories. Heavy ion precipitation was able to reproduce strong X-ray fluxes, but the proposed incident ion energies were very high (>1 MeV/nucleon). Now with the Juno spacecraft at Jupiter, there have been many measurements of heavy ion populations above the polar cap with energies up to 300-400 keV/nucleon (keV/u), well below the ion energies required by earlier models. Recent work has provided a new outlook on how ion-neutral collisions in the Jovian atmosphere are occurring, providing us with an entirely new set of impact cross-sections. The model presented here simulates oxygen and sulfur precipitation, taking into account the new cross-sections, every collision process, the measured ion fluxes above Jupiter's polar aurora, and synthetic X-ray spectra. We predict X-ray fluxes, efficiencies, and spectra for various initial ion energies considering opacity effects from two different atmospheres. We demonstrate an *in situ* measured heavy ion flux above Jupiter's polar cap is capable of producing over 1 GW of X-ray emission when some assumptions are made. Comparison of our approximated synthetic X-ray spectrum produced from *in situ* particle data with a simultaneous X-ray spectrum observed by XMM-Newton show good agreement for the oxygen part of the spectrum, but not for the sulfur part.

1 Introduction

The National Aeronautics and Space Administration's (NASA) Juno mission has, at the time of this writing, been orbiting Jupiter for nearly three years. Since arrival, Juno has arguably uncovered more questions than it has answered, although its discoveries have been numerous. In its time spent at Jupiter, Juno has put greater constraints on the gravitational field (Folkner et al., 2017; Iess et al., 2018), measured a magnetic field with substantial complexity (Connerney et al., 2017, 2018; Moore et al., 2018), and returned images of Jupiter detailing the intricate features seen in the cloud tops (Orton et al., 2017; Sánchez-Lavega et al., 2018). Most importantly to this paper, Juno has been able to measure heavy ions above the polar caps that indicate they are precipitating into the top of the atmosphere (Haggerty et al., 2017; Clark, Mauk, Haggerty, et al., 2017; Clark, Mauk, Paranicas, et al., 2017), potentially producing Jupiter's dynamic X-ray aurorae.

X-ray production at Jupiter has been of interest to the space physics community from when it was first observed by the Einstein Observatory in April of 1979 (Metzger et al., 1983). Although Metzger et al. (1983) were unable to distinguish a line spectrum from a continuum due to the limitations of the detector, they proposed that the primary source of X-rays must be coming from heavy ion precipitation, stating, "the shape of the response and the observed X-ray power indicate that the source of this auroral emission is not electron bremsstrahlung as on the earth, but is most probably line emission from O and S ions with energies between 0.03 and 4.0 MeV/nucleon...". Now, with the Juno spacecraft orbiting Jupiter, oxygen and sulfur ions have been measured above the polar caps with energies up to 400 keV per nucleon (keV/u) (Clark, Mauk, Haggerty, et al., 2017; Clark, Mauk, Paranicas, et al., 2017; Haggerty et al., 2017).

In the past, attempts were made to reproduce the X-ray emission observed at Jupiter with ion precipitation models (Cravens et al., 1995, 2003; Ozak et al., 2010, 2013), but they required very high energy ions (>1.2 MeV/u) to sufficiently strip the ions of their

[c1] *SJH*: ~~Jupiters~~

electrons in order to produce the observed X-ray emissions. But, this could be overlooked because no *in situ* measurements of the ion energies above the polar cap existed. However, such ion measurements are now available thanks to Juno; and a more complete treatment of the underlying atomic collision processes now exists (Schultz et al., 2019). Incorporated into our ion-precipitation models, these new cross-sections demonstrate the "threshold" ion energy necessary to produce X-ray yielding excited states is significantly less (on the order of 200 keV/u) than the earlier cross-sections gave. This difference arises largely from the improved treatment of ion energy loss in the new atomic data, evidenced by an increased stopping power derived from ion-transport simulations for ion energies between 50 and 2000 keV/u that is now in better agreement with recommended values. The more complete treatment also results in a shift in the equilibrium distribution of charge states toward lower energies, and motivated consideration of X-ray production from direct ion excitation in addition to that from charge transfer.

We expand on the ion precipitation models that have come before (Cravens et al., 1995; Houston et al., 2018; Ozak et al., 2010, 2013), modeling oxygen from 10 keV/u to 25 MeV/u and sulfur between 10 keV/u and 2 MeV/u, in an attempt to explain the X-ray emission from the Jovian polar caps. We consider all charge states of oxygen, including the negative charge state (O^{q+}, q=-1, 0, ..., 8), and all sulfur [c1]positive charge states (S^{q+}, q=0, ..., 16). Ultimately, O^{6+}, O^{7+}, and S^{6+}-S^{15+} are the most important charge states to consider when producing X-rays, because their ionization potentials are great enough to emit X-ray photons.

We first discuss the differences between our model and the models by Houston et al. (2018), Ozak et al. (2010), and Ozak et al. (2013). We then introduce new ion-neutral collision processes that account for the vast contrast in our results and those presented by our predecessors. Various techniques used within the model are explained and ion flux measurements made by the Jupiter Energetic Particle Detector Instrument (JEDI) (Mauk et al., 2017) are displayed. Results are given for a variety of monoenergetic ion beam energies, including several ion production rates, X-ray efficiencies, and example X-ray spectra with opacity effects. The JEDI measurements are input into the model and results indicating X-ray production are shown. We compare our modeled spectrum with a simultaneous XMM-Newton spectrum observed during the same window within which the ion precipitation was detected by Juno. Finally, we conclude with a discussion on the implications of the model results.

The observed X-ray aurora has shown a strange complexity. For example, in ∼30% of observations the X-ray aurora pulses with a regular period on the order of 10s of minutes as reported by Dunn et al. (2016, 2017); Gladstone et al. (2002), and Jackman et al. (2018); however, during other observations, the emission is either continuous or the pulses are erratic, with no clear periodic signature (Elsner et al., 2005; Branduardi-Raymont et al., 2007). Therefore, when analyzing heavy ion measurements made by JEDI, it is important to consider that this emission is highly temporally and spatially variable and that the associated ion precipitation may also vary with time. One must remember that every energy spectrum and flux intensity of oxygen and sulfur is unique. Sometimes oxygen fluxes are measured with a higher intensity while at other times sulfur fluxes are higher. Each collection of data greatly depends on the time and location of where it is made. Given that each flight of Juno over the polar regions follows a different flight path, it is also difficult to differentiate spatial and temporal changes in the measurements. Thus, when using the JEDI flux measurements, they need to be fine tuned for every case.

[c1] *SJH-2: Text added.*

2 Physical Processes and Model Description

The basic simulation methods used for this paper have been described in great detail by Ozak et al. (2010, 2013); Houston et al. (2018), and the references therein. When Ozak et al. (2010) first published results, they showed X-ray production rates from precipitating oxygen and sulfur, then Ozak et al. (2013) made predictions of field-aligned currents (FAC) and airglow intensities that Juno would measure when it arrived to Jupiter, and Houston et al. (2018) primarily focused on FAC and ultraviolet (UV) emission from oxygen. We follow up on the promise made in Houston et al. (2018) to include energetic sulfur precipitation and oxygen improvements, with proton precipitation being left to a future and very necessary publication.

Aside from optimization improvements, the main contrast between the current model and earlier versions can be summarized as follows:

- The Jovian atmosphere has been extended deeper, down below the 1 bar level.
- Atomic data (principally inelastic collision cross-sections) for oxygen ions colliding with H_2 previously (Ozak et al., 2013; Schultz et al., 2017) only considered processes that occurred involving electronic transitions of projectile electrons or target electrons non-simultaneously (denoted "NSIM" processes). A more complete treatment for oxygen (Schultz et al., 2019) ion impact expands the model to include simultaneous (SIM) processes that occur involving both target and projectile electron transitions.
- Analogous atomic data for sulfur ion impact of H_2 have also been created (still preliminary and not yet published) that include treatment of SIM processes, updating the purely NSIM processes considered in Ozak et al. (2013), and have been incorporated in the present work from the preliminary analysis of the data to be published.
- X-ray efficiencies and approximations to synthetic X-ray spectra that include opacity effects are presented with both the current atmosphere and an upper limit, fully mixed atmosphere.
- The direct excitation mechanism now also contributes to X-ray production, increasing the number of X-rays produced.
- Juno data (both oxygen and sulfur flux measurements) are adapted and input into the simulation.

2.1 Jovian Atmosphere

Houston et al. (2018) used a neutral atmosphere originally presented by Maurellis and Cravens (2001) based on Galileo probe data (Seiff et al., 1996, 1997) and remote observations (Sada et al., 1998). The same atmosphere is used here, only we have extended the depth from 200 km to -88 km, where 0 km is set to where the pressure is equal to 1 bar (Fig. 1). The atmosphere below 200 km has been generated using temperature-pressure profiles retrieved from NASA's Infrared Telescope Facility and the Texas Echelon Cross Echelle Spectrograph Instrument (IRTF-TEXES) (Sinclair et al., 2018). Using the temperature and pressure, the ideal gas law is then solved to obtain the total number density. Because we are below the homopause, where a well-mixed atmosphere is present, the mixing ratios from 200 km are extended down to -88 km to calculate the number density of each species.

There has been much speculation about the composition of the upper atmosphere over the polar caps (see Section 5.2 of Clark et al. (2018), Gérard et al. (2014), and Parkinson, Stewart, Wong, Yung, and Ajello (2006)). To help account for this, we generate a second atmospheric profile (not displayed) by taking the mixing ratio of molecular hydrogen to helium and methane at the bottom of the density profile in Figure 1 and then redistribute the helium and methane from the top of the atmosphere with that same mix-

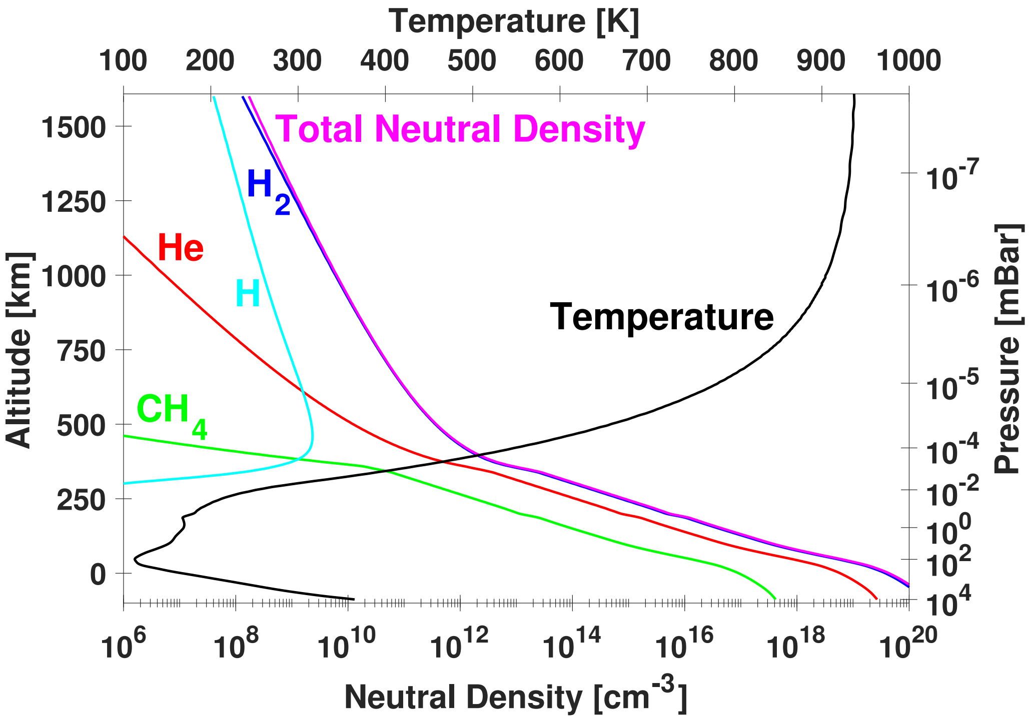

Figure 1. Atmospheric density profiles of H_2, He, CH_4, and H based on data shown in Maurellis and Cravens (2001) and Sinclair et al. (2018). Also shown is the neutral temperature profile as a function of altitude and pressure.

ing ratio. This allows for a completely well-mixed atmosphere that ignores a defined homopause; rather, the entire atmosphere is homogeneous. The H_2 distribution of this atmosphere remains the same as that in Fig 1, thus ion precipitation will not be affected because only ion collisions in a hydrogen gas are considered. However, when photoemission is discussed, the well-mixed atmosphere will have greater photoabsorption effects. Atomic hydrogen is ignored in the well-mixed atmosphere because of how chemically active it tends to be (as can be seen in the original atmosphere, below the homopause) and it is not unreasonable to think the column density of H will have negligible effects on the opacity of X-ray emission, as it does in the original atmosphere. We will refer to the atmosphere displayed in Figure 1 as atmosphere 1 and the well-mixed atmosphere as atmosphere 2.

2.2 Ion-Neutral Impact Processes

Houston et al. (2018) modeled oxygen precipitation using the nine relevant NSIM processes as the ion traversed the upper atmosphere using the atomic data describing the rates of these processes and the energy loss for each process as a function of ion energy given by Schultz et al. (2017), summarized here:

$$O^{q+} + H_2 \rightarrow \begin{cases} O^{q+} + H_2^+ + e & \text{Single Ionization} \\ O^{q+} + 2H^+ + 2e & \text{Double Ionization} \end{cases} \tag{1a}$$

$$O^{q+} + H_2 \rightarrow \begin{cases} O^{(q-1)+} + \begin{cases} H_2^+ & \text{Single Capture} \\ H^+ + H^+ + e & \text{Transfer Ionization} \end{cases} \\ \\ O^{(q-2)+} + \begin{cases} 2H^+ \rightarrow O^{(q-1)+} + e & \text{Double Capture – Autoionization} \\ H^+ + H^+ & \text{Double Capture} \end{cases} \end{cases} \tag{1b}$$

$$O^{q+} + H_2 \rightarrow \begin{cases} O^{(q+1)} + H_2^+ + 2e; H + H^+ + 2e & \text{Single Stripping} \\ O^{(q+2)} + H_2^+ + 3e; H + H^+ + 3e & \text{Double Stripping} \end{cases} \tag{1c}$$

$$O^{q+} + H_2 \rightarrow O^{q+} + H_2^*; H^* + H^* \quad \text{Electronic Excitation - All States} \tag{1d}$$

However, as noted above, treatment of processes that involve electron transitions on both target and projectile simultaneously has subsequently lead to fundamental improvements of the oxygen and sulfur data (Schultz et al., 2019). The NSIM and SIM processes represented by this expanded consideration, utilized in the present ion precipitation model, are the following:

$$\begin{array}{ll}
\mathrm{X}^{q+} + \mathrm{H}_2 \rightarrow \mathrm{X}^{q+} + \mathrm{H}_2^+ + \mathrm{e};\ \mathrm{X}^{q+} + \mathrm{H} + \mathrm{H}^+ + \mathrm{e} & \text{single ionization (SI)} \\
\mathrm{X}^{q+} + \mathrm{H}_2 \rightarrow \mathrm{X}^{q+*} + \mathrm{H}_2^+ + \mathrm{e};\ \mathrm{X}^{q+*} + \mathrm{H} + \mathrm{H}^+ + \mathrm{e} & \text{SI + single projectile excitation (SI+SPEX)} \\
\mathrm{X}^{q+} + \mathrm{H}_2 \rightarrow \mathrm{X}^{q+**} + \mathrm{H}_2^+ + \mathrm{e};\ \mathrm{X}^{q+**} + \mathrm{H} + \mathrm{H}^+ + \mathrm{e} & \text{SI + double projectile excitation (SI+DPEX)} \\
\mathrm{X}^{q+} + \mathrm{H}_2 \rightarrow \mathrm{X}^{(q+1)+} + \mathrm{H}_2^+ + 2\mathrm{e};\ \mathrm{X}^{(q+1)+} + \mathrm{H} + \mathrm{H}^+ + 2\mathrm{e} & \text{SI + single stripping (SI+SS)} \\
\mathrm{X}^{q+} + \mathrm{H}_2 \rightarrow \mathrm{X}^{(q+2)+} + \mathrm{H}_2^+ + 3\mathrm{e};\ \mathrm{X}^{(q+2)+} + \mathrm{H} + \mathrm{H}^+ + 3\mathrm{e} & \text{SI + double stripping (SI+DS)}
\end{array}$$

$$\begin{array}{ll}
\mathrm{X}^{q+} + \mathrm{H}_2 \rightarrow \mathrm{X}^{q+} + \mathrm{H}^+ + \mathrm{H}^+ + 2\mathrm{e} & \text{double ionization (DI)} \\
\mathrm{X}^{q+} + \mathrm{H}_2 \rightarrow \mathrm{X}^{q+*} + \mathrm{H}^+ + \mathrm{H}^+ + 2\mathrm{e} & \text{DI+SPEX} \\
\mathrm{X}^{q+} + \mathrm{H}_2 \rightarrow \mathrm{X}^{q+**} + \mathrm{H}^+ + \mathrm{H}^+ + 2\mathrm{e} & \text{DI+DPEX} \\
\mathrm{X}^{q+} + \mathrm{H}_2 \rightarrow \mathrm{X}^{(q+1)+} + \mathrm{H}^+ + \mathrm{H}^+ + 3\mathrm{e} & \text{DI+SS} \\
\mathrm{X}^{q+} + \mathrm{H}_2 \rightarrow \mathrm{X}^{(q+2)+} + \mathrm{H}^+ + \mathrm{H}^+ + 4\mathrm{e} & \text{DI+DS}
\end{array}$$

$$\begin{array}{ll}
\mathrm{X}^{q+} + \mathrm{H}_2 \rightarrow \mathrm{X}^{(q-1)+} + \mathrm{H}^+ + \mathrm{H}^+ + \mathrm{e} & \text{transfer ionization (TI)} \\
\mathrm{X}^{q+} + \mathrm{H}_2 \rightarrow \mathrm{X}^{(q-1)+*} + \mathrm{H}^+ + \mathrm{H}^+ + \mathrm{e} & \text{TI+SPEX} \\
\mathrm{X}^{q+} + \mathrm{H}_2 \rightarrow \mathrm{X}^{(q-1)+**} + \mathrm{H}^+ + \mathrm{H}^+ + \mathrm{e} & \text{TI+DPEX} \\
\mathrm{X}^{q+} + \mathrm{H}_2 \rightarrow \mathrm{X}^{q+} + \mathrm{H}^+ + \mathrm{H}^+ + 2\mathrm{e} & \text{TI+SS} \\
\mathrm{X}^{q+} + \mathrm{H}_2 \rightarrow \mathrm{X}^{(q+1)+} + \mathrm{H}^+ + \mathrm{H}^+ + 3\mathrm{e} & \text{TI+DS}
\end{array}$$

$$\begin{array}{ll}
\mathrm{X}^{q+} + \mathrm{H}_2 \rightarrow \mathrm{X}^{(q-2)+**} + \mathrm{H}^+ + \mathrm{H}^+ \rightarrow \mathrm{X}^{(q-1)+} + \mathrm{e} & \text{double capture autionization (DCAI)} \\
\mathrm{X}^{q+} + \mathrm{H}_2 \rightarrow \mathrm{X}^{(q-2)+***} + \mathrm{H}^+ + \mathrm{H}^+ \rightarrow \mathrm{X}^{(q-1)+*} + \mathrm{e} & \text{DCAI+SPEX} \\
\mathrm{X}^{q+} + \mathrm{H}_2 \rightarrow \mathrm{X}^{(q-2)+****} + \mathrm{H}^+ + \mathrm{H}^+ \rightarrow \mathrm{X}^{(q-1)+**} + \mathrm{e} & \text{DCAI+DPEX} \\
\mathrm{X}^{q+} + \mathrm{H}_2 \rightarrow \mathrm{X}^{(q-2)+**} + \mathrm{H}^+ + \mathrm{H}^+ \rightarrow \mathrm{X}^{q+} + 2\mathrm{e} & \text{DCAI+SS} \\
\mathrm{X}^{q+} + \mathrm{H}_2 \rightarrow \mathrm{X}^{(q-2)+**} + \mathrm{H}^+ + \mathrm{H}^+ \rightarrow \mathrm{X}^{(q+1)+} + 3\mathrm{e} & \text{DCAI+DS}
\end{array}$$

$$\begin{array}{ll}
\mathrm{X}^{q+} + \mathrm{H}_2 \rightarrow \mathrm{X}^{(q-1)+} + \mathrm{H}_2^+;\ \mathrm{X}^{(q-1)+} + \mathrm{H} + \mathrm{H}^+ & \text{single electron capture (SC)} \\
\mathrm{X}^{q+} + \mathrm{H}_2 \rightarrow \mathrm{X}^{(q-1)+*} + \mathrm{H}_2^+;\ \mathrm{X}^{(q-1)+*} + \mathrm{H} + \mathrm{H}^+ & \text{SC+SPEX} \\
\mathrm{X}^{q+} + \mathrm{H}_2 \rightarrow \mathrm{X}^{(q-1)+**} + \mathrm{H}_2^+;\ \mathrm{X}^{(q-1)+**} + \mathrm{H} + \mathrm{H}^+ & \text{SC+DPEX} \\
\mathrm{X}^{q+} + \mathrm{H}_2 \rightarrow \mathrm{X}^{q+} + \mathrm{H}_2^+ + \mathrm{e};\ \mathrm{X}^{q+} + \mathrm{H} + \mathrm{H}^+ + \mathrm{e} & \text{SC+SS} \\
\mathrm{X}^{q+} + \mathrm{H}_2 \rightarrow \mathrm{X}^{(q+1)+} + \mathrm{H}_2^+ + 2\mathrm{e};\ \mathrm{X}^{(q+1)+} + \mathrm{H} + \mathrm{H}^+ + 2\mathrm{e} & \text{SC+DS}
\end{array}$$

$$\begin{array}{ll}
\mathrm{X}^{q+} + \mathrm{H}_2 \rightarrow \mathrm{X}^{(q-2)+} + \mathrm{H}^+ + \mathrm{H}^+ & \text{double electron capture (DC)} \\
\mathrm{X}^{q+} + \mathrm{H}_2 \rightarrow \mathrm{X}^{(q-2)+*} + \mathrm{H}^+ + \mathrm{H}^+ & \text{DC+SPEX} \\
\mathrm{X}^{q+} + \mathrm{H}_2 \rightarrow \mathrm{X}^{(q-2)+**} + \mathrm{H}^+ + \mathrm{H}^+ & \text{DC+DPEX} \\
\mathrm{X}^{q+} + \mathrm{H}_2 \rightarrow \mathrm{X}^{(q-1)+} + \mathrm{H}^+ + \mathrm{H}^+ + \mathrm{e} & \text{DC+SS} \\
\mathrm{X}^{q+} + \mathrm{H}_2 \rightarrow \mathrm{X}^{q+} + \mathrm{H}^+ + \mathrm{H}^+ + 2\mathrm{e} & \text{DC+DS}
\end{array}$$

$X^{q+} + H_2 \rightarrow X^{q+} + H_2^*$	target excitation (TEX)
$X^{q+} + H_2 \rightarrow X^{q+*} + H_2^*$	TEX+SPEX
$X^{q+} + H_2 \rightarrow X^{q+**} + H_2^*$	TEX+DPEX
$X^{q+} + H_2 \rightarrow X^{(q+1)+} + H_2^* + e$	TEX+SS
$X^{q+} + H_2 \rightarrow X^{(q+2)+} + H_2^* + 2e$	TEX+DS

where X stands for the projectile, either O or S. q is the charge state and depends on the number of electrons bound to the ion; q runs from 0 to 8 for O and from 0 to 16 for S. The abbreviations for each process shown here are used throughout the rest of the paper. Some processes are not possible for neutral or singly ionized atoms or, similarly, for fully stripped or O^{7+} and S^{15+} ions (e.g., for neutral O and S capture of two electrons, DC, cannot occur and for the fully stripped ions O^{8+} and S^{16+}, neither single or double stripping, SS or DS, is possible). We also include the negative ion channel, that is, production and destruction of O^-, as described by Schultz et al. (2019), owing to the importance to the charge state distribution at low energy, and implications for its presence in atmospheric chemical models. We use a single, NSIM process that can bring O to O^-, governed by the cross-sections in Table C of Schultz et al. (2019). Once in the negative charge state, six processes are considered; SI, SI+SS, DI, DI+SS, TEX, and TEX+SS. For more details, see Section 3.4 *Auxiliary data model* given by Schultz et al. (2019). [c1]Furthermore, S^- was not calculated because the importance of that channel to the ion fraction populations of S, S^+, and possibly S^{2+} were not realized at the time of the calculations, but subsequently identified for O^- production (Schultz et al., 2019)[c2] for which explicit measurements exist for the ion fraction distributions of O^-, O, O^+, and O^{2+} to test inclusion of the O^- production and destruction channels. For the present work, inclusion of the corresponding channels for S^- would be relevant for only the lowest energy portion of the ion energy range considered, not significantly affecting the energy loss and ion fraction population except at the lowest portion of this energy range and not significantly influencing the x-ray production (little comes from excitation of S or S+ at these low impact energies).

Details of the atomic collision model and calculations have been given by Schultz et al. (2019) as well as explanation of the improvements to ion and electron transport models due to inclusion of SIM processes. As noted above, important for the present work is the fact that the more complete atomic collision model has shifted the peaks of the ion charge state distribution to lower ion energies and has motivated consideration of the additional X-ray production mechanism, direct projectile excitation, in addition to the previously considered X-ray emission subsequent to charge transfer.

2.3 Charge State Equilibrium Fractions

In a very broad sense, as an ion precipitates through the atmosphere each collision with an atmospheric gas molecule or atom can result in four different outcomes for the projectile. The ion can become excited through NSIM or SIM processes (e.g. SPEX or SPEX+SI), become further ionized (e.g. NSIM or SIM SS or DS), gain an electron or two (e.g. NSIM or SIM SC or TI), or can maintain its charge while [c3]affecting the target (e.g. NSIM SI or TEX). Each type of interaction is governed by the energy of the precipitating ion; that is, a more energetic ion will generally be stripped of more electrons than one precipitating with less energy. By knowledge of the stripping and charge transfer cross-sections, it is possible to calculate the equilibrium fractions of each charge state versus the ion energy. This is done using transition probabilities, P_{ij}:

$$\phi_q^i(E)P_{q,q+1}^i = \phi_{q+1}^i(E)P_{q+1,q}^i \tag{2}$$

[c1] *SJH-2*: *Text added.*
[c2] *SJH-2*: *Text added.*
[c3] *SJH-1*: ~~effecting~~

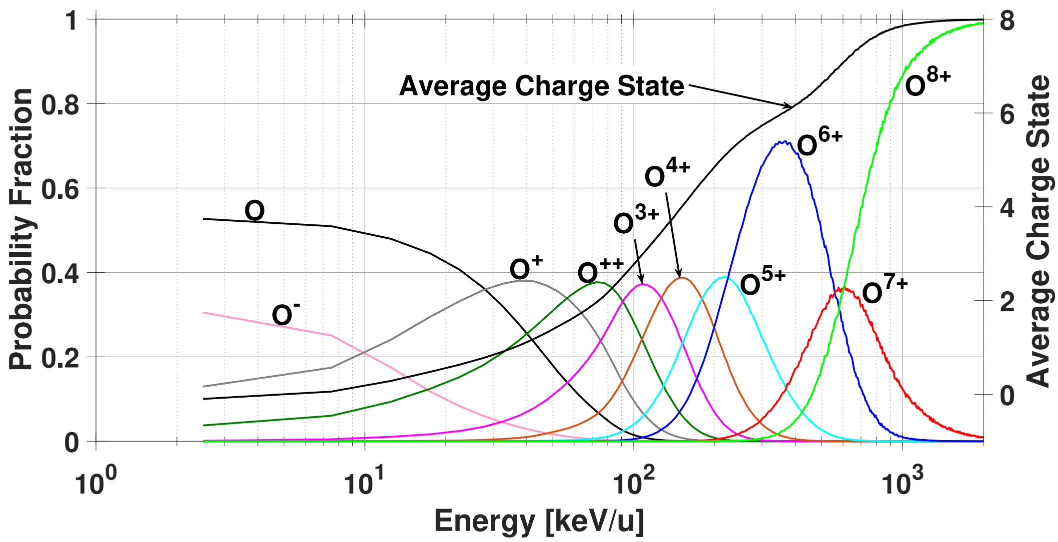

Figure 2. Oxygen charge state distribution as a function of ion energy. The high charge state peaks have dramatically shifted to lower energies than previous models produced. Houston et al. (2018) and Ozak et al. (2010) had the peak of O^{6+} at ~900 keV/u; however, due to the use of newly developed SIM cross-sections, the peak has now shifted down to an energy of ~350 keV/u.

where $\phi^i_q(E)$ is the fraction of ions in charge state q, at energy E, for species i, either oxygen or sulfur. $P^i_{q,q+1}$ denotes the sum of the stripping cross-sections and $P^i_{q+1,q}$, the sum of the charge transfer cross-sections, for species i. A normalization is given by the condition of each energy

$$\sum_{q=q_0}^{q=Z} \phi^i_q(E) = 1 \tag{3}$$

where q_0 denotes the lowest charge state for species i, q_0=-1 for O and q_0=0 for S, Z=8,16 are the nuclear charges for O and S, and $\phi^i_q(E)$ is the charge state fraction. These are shown for oxygen and sulfur as a function of energy in Figures 2 and 3.

The charge state equilibrium fractions demonstrate at what energy the ion will reach a given charge state regardless of the sequence of collision processes undergone or the initial ion energy; the ion history is immediately forgotten. From these fractions one can quickly see what energies are required for an ion to begin producing X-rays. For both oxygen and sulfur the sixth charge state must be reached to begin producing X-rays (O^{6+} and S^{6+} with projectile excitation, or O^{7+} and S^{7+} via charge exchange). These charge states are sufficiently reached for both species at an energy between 200-300 keV/u, where they become the most probable charge state for the given energy (a total energy of ~3.2 MeV and ~6.4 MeV for oxygen and sulfur, respectively). These newly developed equilibrium fractions supersede previous models presented by Ozak et al. (2010) and Houston et al. (2018), which showed an O^{6+} peak at nearly 1 MeV/u and an S^{6+} peak at 600 keV/u.

Relative to the previous results it now requires less energy to produce charge states capable of emitting X-rays and the ions are not penetrating the atmosphere as deeply as was previously modeled because more energy is being lost in the middle energy range (between 50 and 2000 keV/u; see the stopping power discussion given by Schultz et al. (2019)), affecting the depth effects and predicted X-ray spectra.

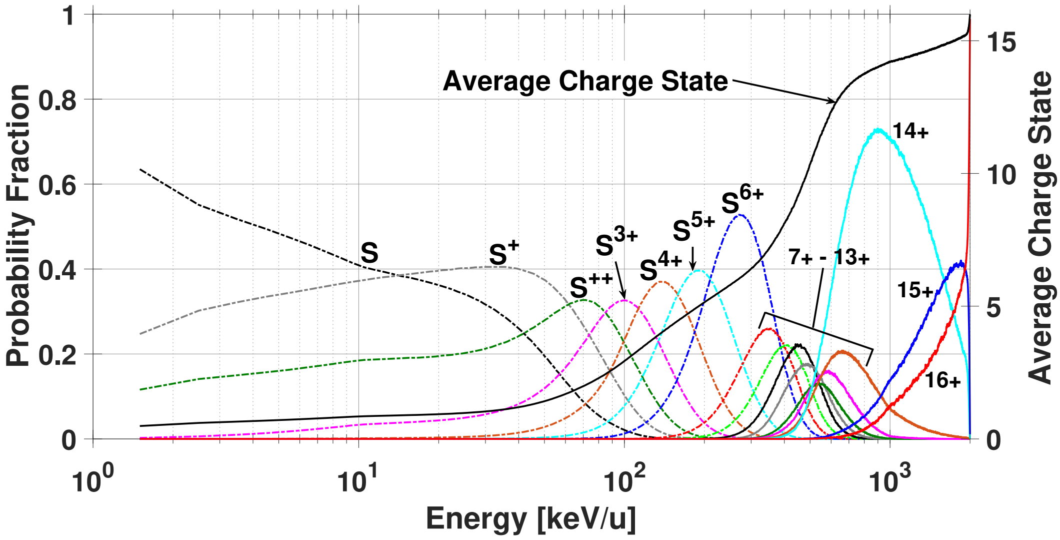

Figure 3. Sulfur charge state distribution as a function of ion energy. The high charge state peaks have dramatically shifted to lower energies than previous models produced. Ozak et al. (2010) had the peaks of S^{6+} and S^{14+} at ~500 keV/u and ~2.2 MeV/u, respectively. Due to the use of newly developed SIM cross-sections, the peaks have now shifted down to energies of ~275 keV/u and ~900 keV/u, respectively.

2.4 Depth Effects

The opacity of the Jovian atmosphere is incorporated into the model using the optical depth of outgoing X-ray photons. We look at three different path angles, 0°, 80°, and 90° (where the angle is measured with respect to the axis of rotation), and with two atmospheric profiles; the density profile shown in Figure 1 and a well-mixed atmosphere as discussed in Section 2.1. The optical depth is given by

$$\tau(\lambda, z_0) = Ch(\theta, z_0) \sum_j \sigma_j^{abs}(\lambda) \int_{z_0}^{\infty} n_j(z) dz \tag{4}$$

where $\tau(\lambda, z_0)$ is the optical depth as a function of emitted photon wavelength, λ, and the altitude at which the emission occurred, z_0. $Ch(\theta, z_0)$ is the Chapman function, dependent upon the photon path angle, θ, and the altitude. $\sigma_j^{abs}(\lambda)$ is the absorption cross-section summed over each species, j (H_2, He, and CH_4), and is a function of wavelength. For example, the absorption cross-section at a photon energy of 100 eV is 3.7x10^{-20}, 2.8x10^{-19}, and 4.4x10^{-19}, for H_2, He, and CH_4, respectively, and continues to decrease in value through 10 keV (with the exception of a sharp spike in CH_4 at 283 eV[c1], due to the K-shell edge) (Cravens et al., 2006)[c2]. $n_j(z)$ is the neutral density of each atmospheric constituent as a function of altitude, integrated from the point of emission out through the top of the atmosphere.

[c1] *SJH-2*: *Text added.*
[c2] *SJH-2*: Changed from Cravens et al., 1995

[c3]At angles between 0° and 80°, the Chapman function has been approximated to[c4c5]: [c6]

$$Ch(0^\circ \leq \theta \leq 80^\circ, z_0) \approx \sec(\theta) \tag{5}$$

and [c1]since this approximation tends toward infinity for $\theta = 90^\circ$, for this case we then use:

$$Ch(\frac{\pi}{2}, z_0) = \sqrt{\frac{R_J}{H(z_0)}\frac{\pi}{2}} \tag{6}$$

[c2]where R_J is the Jovian radii of 71,492 km and $H(z_0)$ is the scale height at altitude z_0. The spectrum intensity, $4\pi I(\lambda)$ can then be calculated as

$$4\pi I(\lambda) = \int_{z_0}^{\infty} P(\lambda, z) e^{-\tau(\lambda, z_0)} dz \tag{7}$$

where $P(\lambda, z)$ is the production rate of X-ray emission as a function of wavelength, λ and altitude, z. z_0 is the deepest altitude that is reached by the ion beam before all of its energy is deposited into the atmosphere and $\tau(\lambda, z_0)$ is the aforementioned optical depth.

$P(\lambda, z)$ integrated over every value of λ is equal to the ion production rate, $P(z)$, and can be calculated for a given ion charge state. Therefore, to determine the production rate as a function of wavelength there are a couple of things to note before building an approximate synthetic spectra.

2.5 Approximated Synthetic X-ray Spectra

An X-ray can be emitted through either the ion gaining an electron (what we refer to as a charge transfer or charge exchange collision) or the excitation of the ion (called direct excitation). Both of these scenarios result in one or more electrons in an excited state followed by emission of a photon as the electron(s) cascade down to a lower energy state. Although there are many charge transfer and projectile excitation processes we only allow three of each type to ultimately result in the emission of a photon: TI, SC, and SC+SS for charge exchange and SI+SPEX, DI+SPEX, and TEX+SPEX for direct excitation. Any collisions that result in more than one electron being in an excited state at a given time, whether it be through charge exchange, projectile excitation, or a combination of the two (e.g. DC or SC+SPEX collisions), we consider it much more likely for the Auger effect (the energy being given to an ejected electron) to take place than the emission of a photon.

Due to the lack of published[c3] X-ray emission cascade models, and, given the distribution of electronic excitation given by our ion-precipitation model, we have adopted synthetic spectra resulting from charge transfer for O and S ions by Hui et al. (2010)[c4]. These spectra are available only at ion energies somewhat above those needed here, owing to the shift of the charge state distributions to lower energies from use of the SIM processes model. [c5]Using the data available from Hui et al. (2010), we have produced an approximated spectra vs. number of photons/ion which we have re-normalized for

[c3] *SJH-2*: ~~The~~
[c4] *SJH-2*: ~~$Ch(0^\circ \leq \theta \leq 80^\circ, z_0) \approx \sec(\theta)$ for the first two exit angles~~
[c5] *SJH-2*: *Text added.*
[c6] *SJH-2*: Changed to make into an equation.
[c1] *SJH-2*: *Text added.*
[c2] *SJH-2*: ~~for θ=90^0,~~
[c3] *SJH-1*: ~~, available X-ray emission cascade models~~
[c4] *SJH-1*: ~~available only at ion energies somewhat above those needed here (owing to the shift of the charge state distributions to lower energies from use of the SIM processes model)~~
[c5] *SJH-1*: ~~From~~

each charge state to the total number of photons/charge state. We then multiplied the ion production from charge exchange produced by our model, $P(z)$, by the normalized emission lines to generate $P(\lambda, z)$.

[c1]We do not have any state-selective excitation emission spectra of oxygen and sulfur for direct excitation; instead we apply an approximation to the charge exchange emission lines we do have available. In general, energy levels reached by excitation of the projectile ion will be predominantly to lower levels than those from charge transfer. Charge transfer proceeds to states with principal quantum number n peaked at $\approx q^{3/4}$ (Grozdanov & Janev, 1978; Olson, 1981), with a distribution below and above this, falling off at high quantum number as $1/n^3$ (Oppenheimer, 1928; Schultz et al., 2010). In contrast, excitation proceeds dominantly to the next highest n-level and rapidly falls off for higher n. (Note: [c2]Another consideration is forbidden excitation transitions for each charge state; however, that requires a much more in-depth study of the situation beyond the scope of the research presented here.) Thus, we have approximated the excitation to the next highest n-level as 80-85%, the possibility of excitation of two n-levels as 15%, and to a third higher excitation level as 0-5%.

To do this, we take the two or three most common emission lines, at lower photon energies, from the charge exchange synthetic spectra provided by Hui et al. (2010) and distribute the direct excitation emission in the following way

$$\sum_{i=1}^{2,3} \frac{hc}{\lambda_i} f_i = E \tag{8}$$

where h is Planck's constant, c is the speed of light, and λ_i is the wavelength of the most likely emission line, or group of emission lines. If there is a group of emission lines with similar wavelengths ($\Delta\lambda \approx 10$ eV), the emission is distributed evenly among each wavelength because in this simple approximation we do not know the exact state-selective excitation transitions, and forbidden excitation states have not been considered. f_i is the distribution of X-ray production given to each wavelength. If only two lines[c3] (or groups of lines) are considered then f_1=0.85 and f_2=0.15; for three, f_1=0.80, f_2=0.15, and f_3=0.05. E is the total photon energy from emission.

To ensure this approximation is not violating conservation of energy, if the emitted photon energy is greater than the energy loss for single projectile excitation (SPEX), $E > \Delta E$, where ΔE is the energy loss for SPEX at a given ion energy and charge state shown in Schultz et al. (2019), then the emission given in Equation 8 is re-normalized to conserve energy,

$$\sum_{n=1}^{2,3} \frac{hc}{\lambda_n} f_n \epsilon = E \tag{9}$$

where $\epsilon = \Delta E/E$. If $E < \Delta E$ then we keep the distribution as is and assume the energy difference is due to emission from lower energy photons not considered in the X-ray spectrum and X-ray inefficiencies in emission from the way the electrons cascade through the electron orbitals.

To produce a more realistic approximate synthetic spectrum comparable with observation [c4]that an X-ray observatory would detect, we apply a normalized Gaussian distribution to each data point to simulate instrumental response functions, recovering a

[c1] *SJH-1*: ~~Unfortunately, we~~
[c2] *SJH-1*: ~~A second thing to consider would be~~
[c3] *SJH-1*: ~~, or groups of lines,~~
[c4] *SJH-1*: ~~as opposed to infinitely narrow line emission~~

new intensity:

$$4\pi I'(\lambda) = \sum_{\lambda_\mu} \frac{1}{\sqrt{2\pi\sigma^2}} I(\lambda) e^{-\frac{(\lambda-\lambda_\mu)^2}{2\sigma^2}} \tag{10}$$

where λ is now the full spectrum (in eV) which we allow to range from 100 eV to 3500 eV. λ_μ is the wavelength of each emission line and σ^2 is the variance, where σ=20 eV. A careful data-model comparison requires instrument response functions (e.g. for CXO or XMM-Newton).

2.6 Juno Data

With recent measurements from JEDI (Mauk et al., 2017) on the Juno spacecraft, we have obtained heavy ion flux measurements above Jupiter's polar caps indicating both oxygen and sulfur precipitation (Haggerty et al., 2017; Clark, Mauk, Haggerty, et al., 2017; Clark, Mauk, Paranicas, et al., 2017). We input these measurements into our model and produce expected observables for a given flux. For this study, we use [c1]downward precipitating heavy ion measurements from a northern auroral pass during Perijove (PJ) 7 on July 11, 2017, displayed in Figure 4. [c2]These measurements are taken during a time when Juno's magnetic footprint is leaving the polar cap and crossing equatorward over the main auroral oval.

Re-normalization and interpolation of all of the data is necessary to make the flux compatible with the ion precipitation model. The re-normalization requires multiplying the measured intensity by the JEDI energy bin widths (Mauk et al., 2017) and 2π to obtain a flux in ions/cm^2/s. The first three energy bins (170.7, 240.2, and 323.6 keV) on the JEDI instrument are unable to distinguish between oxygen and sulfur, but fortunately these low energy bins will not contribute to X-ray production. We then use a simple linear interpolation to give the data finer resolution so the results are smoother, although it has no effect on the total X-ray production. These flux measurements are then used as an input ion flux into our model, or more simply, one can multiply the output from various monoenergetic runs (which are normalized to an input of 1 ion/cm^2/s) by the re-normalized flux given by JEDI.

It is important to note that although the low energy bins are unable to distinguish between oxygen and sulfur, the higher energy bins of JEDI make separate oxygen and sulfur measurements, and in the case presented, oxygen happens to be more abundant. This is not necessarily a typical measurement and, as suggested by X-ray observation, we generally expect sulfur to produce higher concentrations of X-ray emission. Data have indicated that the sulfur to oxygen (S:O) ratio varies between measurements (Delamere et al., 2005; Dougherty et al., 2017; Kim et al., 2019) which needs to be considered when comparing approximated synthetic X-ray spectra with that from observation. Figure 4 has an S:O ratio of about 0.8 which is a mid-range ratio presented by Radioti et al. (2005, 2006), where the S:O ratio is shown to vary between 0.3-1.2.

Jupiter's X-ray aurora is known to be highly time variable. The X-ray aurora pulses/flares on timescales of a few minutes, while the power output from the aurora can vary by a factor of a few from rotation to rotation (0.5 - 2 GW) and the spectrum is known to change significantly on similar timescales (e.g. Branduardi-Raymont et al. (2007); Elsner et al. (2005); Hui et al. (2010)). The spatial location of the emission may also vary across the auroral zone (Dunn et al., 2017; Gladstone et al., 2002; Jackman et al., 2018), with some suggestion that sulfur X-ray lines may be brighter at lower auroral latitudes (Dunn et al., 2016).

[c1] *SJH-1: Text added.*
[c2] *SJH-1: Text added.*

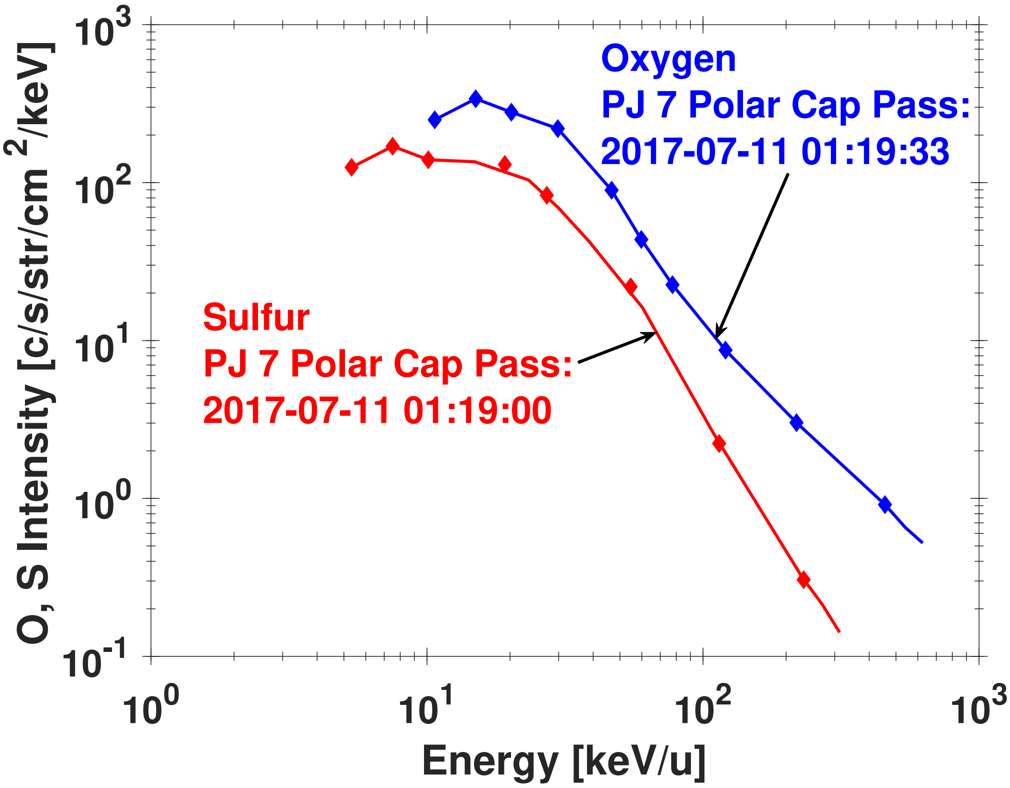

Figure 4. [c4]Downward precipitating oxygen and sulfur flux measurements from JEDI on the Juno spacecraft during Perijove 7. The points marked with a diamond are the actual JEDI measurements. The lines represents the interpolation of the data that we applied to the measurements. Note the power law distribution seen in both species; however, oxygen appears to have an extended high energy tail when compared with sulfur.

3 Results

3.1 Ion Production Rates

When referring to ion production rates here, we are only focusing on production from charge transfer collisions, i.e. $X^q \rightarrow X^{q-1}$, and not stripping collisions, which change[c1] the charge state in the opposite direction. [c2]We will only consider the ion production rate from the collisions that [c3]produce photons, [c4]i.e., mainly TI, SC, and SC+SS. Furthermore, the ion production rate as a function of altitude, $P(z)$, can be calculated outright for a product ion species, i, (e.g. O^{7+} or S^{8+}) as follows:

$$P(z) = n(z)[\sigma^i_{q,q-1}(E(z))]\phi^i_q \Phi^i \tag{11}$$

where $n(z)$ is the neutral atmosphere density of H_2, $\sigma^i_{q,q-1}(E(z))$ denotes the charge transfer cross-sections for species i with energy E at altitude z, ϕ^i_q is the equilibrium fraction given in Equations 2 and 3, and Φ^i represents the total flux of the initial ion beam. However, our model uses a Monte Carlo method that tracks each ion individually and counts each charge exchange collision that occurs for a given charge state. These collisions are tracked through a set of altitude bins with a given input of ∼20,000 incident ions and then the production rate is normalized to an input of 1 ion/cm^2/s. The production rates as a function of H_2 density and altitude for O^{6+} and O^{7+} are shown in Figure 5. For sulfur, Figure 6 shows the S^{7+} and S^{8+} charge transfer production rates. It is to be emphasized, these production rates only include charge exchange from the three [c5]collisional processes discussed in Section 2.5, that is TI, SC, and SC+SS; although other processes can contribute to lowering the overall charge state without emitting a photon (e.g. the Auger process). The altitude integrated production rates for every charge state and various initial ion energies can be found in Appendices A and B, including the production rate of directly excited ions. It is worth noting that[c6], for sulfur, these results use preliminary data[c7], [c8]and may be subject to revision.

It is evident [c9]from Figures 5[c10] and 6 that the production rate of X-ray producing charge states from charge exchange collisions, O^{6+} and S^{7+}, is obtained with energies as low as 200 keV/u, which is well within the range of ion energies measured by Juno above the polar caps (Haggerty et al., 2017; Clark, Mauk, Haggerty, et al., 2017; Clark, Mauk, Paranicas, et al., 2017).

3.2 X-ray Efficiencies

The emitted photon flux is determined by using the production rates, shown in Figures 5 and 6, and Equation 7, where 4π is included to convert the intensity units from cm^{-2} s^{-1} sr^{-1} to cm^{-2} s^{-1}. X-ray emission efficiency is a way of quantifying how many photons are emitted given an incident ion energy and is found by dividing $4\pi I$ by the initial energy of the monoenergetic ion beam. Table 1 shows the combined X-ray efficiencies from both charge exchange and direct excitation emission given an incident ion energy, at various viewing angles, using both atmosphere 1 and 2, and with an input of 1 ion/cm^2/s. The same is also shown in Figures 7 and 8. Given the approximations noted above to infer the electron state populations from charge transfer and projectile excita-

---

[c1] *SJH-1*: ~~s~~
[c2] *SJH-1*: ~~At times, w~~
[c3] *SJH-1*: ~~we believe~~
[c4] *SJH-1*: *Text added.*
[c5] *SJH-1*: ~~collisions~~
[c6] *SJH-1*: *Text added.*
[c7] *SJH-1*: *Text added.*
[c8] *SJH-1*: ~~that will subsequently be checked and refined prior to publication~~
[c9] *SJH-1*: *Text added.*
[c10] *SJH-1*: *Text added.*

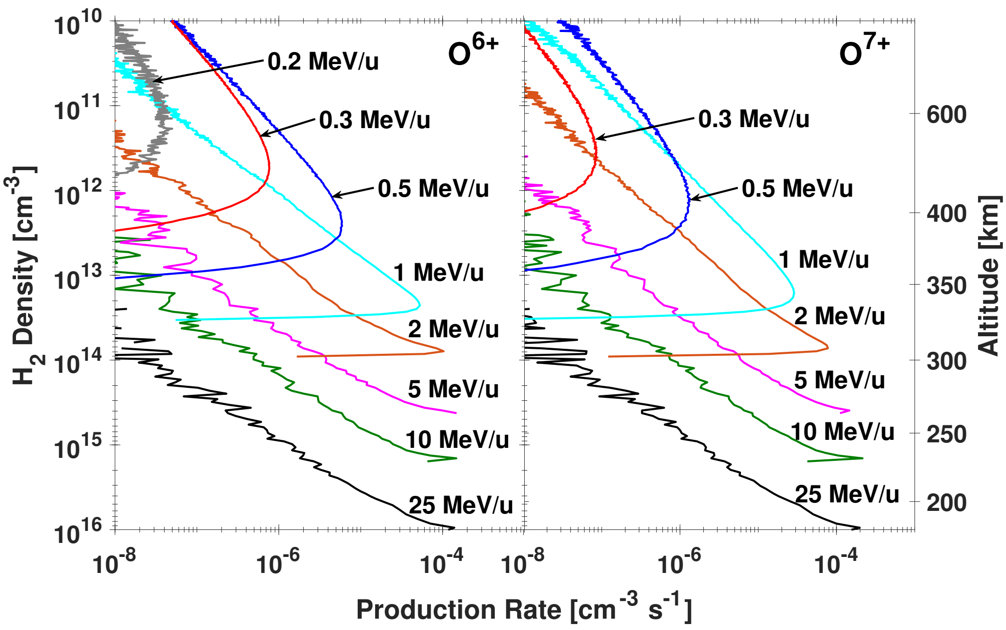

Figure 5. The O^{6+} and O^{7+} production rates from TI, SC, and SC+SS vs. H_2 density and altitude for various incident ion energies (E=0.2, 0.3, 0.5, 1.0, 2.0, 5.0, 10.0, and 25.0 MeV/u). The production rates have been normalized to a single incident ion/cm^2/s.

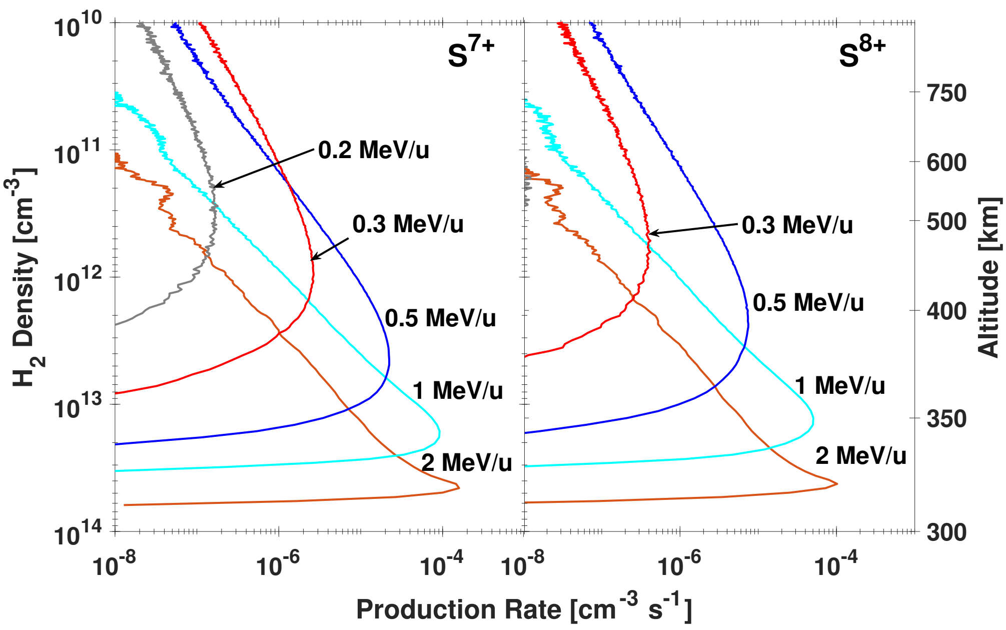

Figure 6. The S^{7+} and S^{8+} production rates from TI, SC, and SC+SS vs. H_2 density and altitude for various incident ion energies (E=0.2, 0.3, 0.5, 1.0, and 2.0 MeV/u). The production rates have been normalized to a single incident ion/cm^2/s.

Atmosphere 1 (Original atmosphere)

Energy	0°				90°			
[keV/u]	O^{6+}	O^{7+}	S^{8+}	S^{9+}	O^{6+}	O^{7+}	S^{8+}	S^{9+}
200	0.0141	0.0005	0.0023	0.0001	0.0139	0.0005	0.0019	0.0001
300	0.1195	0.0106	0.0514	0.0085	0.1165	0.0104	0.0365	0.0072
400	0.2008	0.0317	0.2093	0.0745	0.1901	0.0309	0.1195	0.0563
500	0.2669	0.0735	0.3208	0.1882	0.2358	0.0701	0.1327	0.1206
600	0.2884	0.1206	0.3020	0.2145	0.2235	0.1107	0.0772	0.1022
700	0.2787	0.1578	0.2557	0.1924	0.1760	0.1357	0.0370	0.0589
800	0.2573	0.1810	0.2169	0.1663	0.1240	0.1409	0.0185	0.0300
900	0.2333	0.1911	0.1858	0.1443	0.0827	0.1303	0.0106	0.0157
1000	0.2105	0.1918	0.1608	0.1265	0.0551	0.1118	0.0069	0.0093
2000	0.0954	0.1244	0.0527	0.0474	0.0029	0.0128	0.0009	0.0009

Atmosphere 2 (Well-mixed atmosphere)

Energy	0°				90°			
[keV/u]	O^{6+}	O^{7+}	S^{8+}	S^{9+}	O^{6+}	O^{7+}	S^{8+}	S^{9+}
200	0.0140	0.0005	0.0022	0.0001	0.0134	0.0005	0.0015	0.0001
300	0.1192	0.0106	0.0507	0.0084	0.1068	0.0100	0.0267	0.0057
400	0.2000	0.0317	0.2048	0.0736	0.1643	0.0289	0.0799	0.0418
500	0.2653	0.0733	0.3113	0.1849	0.1867	0.0633	0.0792	0.0817
600	0.2861	0.1201	0.2904	0.2093	0.1606	0.0954	0.0397	0.0600
700	0.2761	0.1570	0.2441	0.1864	0.1156	0.1111	0.0170	0.0297
800	0.2545	0.1799	0.2060	0.1602	0.0756	0.1096	0.0084	0.0138
900	0.2307	0.1898	0.1760	0.1386	0.0478	0.0967	0.0050	0.0072
1000	0.2080	0.1904	0.1521	0.1212	0.0311	0.0802	0.0033	0.0044
2000	0.0942	0.1234	0.0498	0.0453	0.0017	0.0087	0.0006	0.0006

Table 1. The X-ray efficiency ($[\mathrm{cm}^2\mathrm{sec}]^{-1}[\mathrm{keV/u}]^{-1}$) of outgoing photons as a function of initial ion energy including opacity effects from a single incident ion/cm^2/s with an isotropic downward distribution of pitch angles. The viewing angles of 0° and 90° are displayed for both atmosphere 1 and 2. The efficiencies shown here include X-ray production from both charge exchange and direct excitation collisions.

tion, the full set of efficiencies for every X-ray emitting charge state at each energy and three different viewing angles plus a no opacity case can be found in Appendices A and B.

The most efficient X-ray emission for O^{6+} is with an incident ion energy of ∼600 keV/u for both atmospheres, ∼1 MeV/u for O^{7+}, ∼500 keV/u S^{8+}, and ∼600 keV/u for S^{9+}. The well-mixed atmosphere has minimal effects on emission from low energy ion precipitation because the ions are not precipitating deeply enough for the large column density to have much of an impact on the X-rays. As one would expect, the viewing angle of 90° greatly reduces emission for high energy ion precipitation when comparing with X-rays that propagate directly up and out of the atmosphere at 0°. This is even more true for X-ray production from sulfur which is the overall most efficient X-ray producer (i.e., S^{8+} at 500 keV/u) with a viewing angle of 0°, but the efficiency is reduced by nearly 60% (for atmosphere 1) when the viewing angle changes to 90°, whereas O^{6+} is only reduced by about 23% (for atmosphere 1) making it the most efficient emitter at 90°. This is an important effect to consider when looking at fluxes from earth-orbit-based X-ray observations, which are generally taken at a steep viewing angle, especially for the southern aurora.

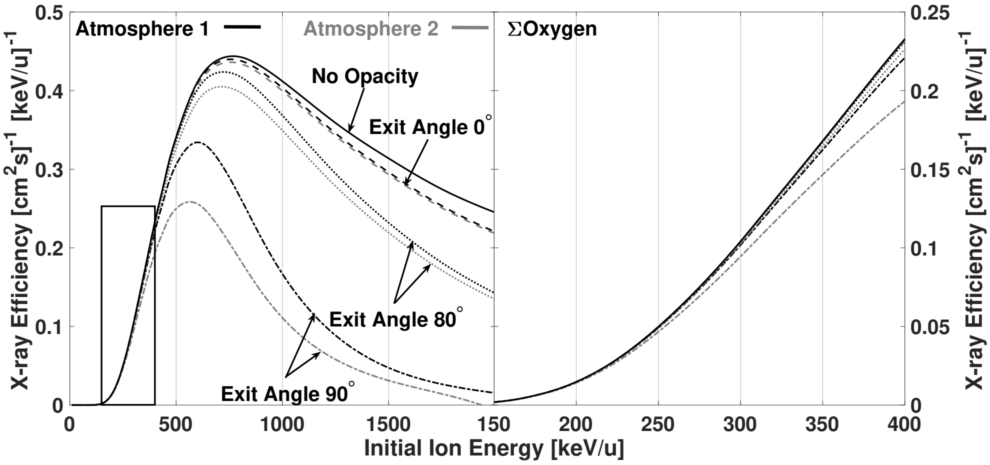

Figure 7. The entire outgoing X-ray flux efficiency for all X-ray producing oxygen charge states as a function of initial ion energy from a single incident ion/cm^2/s with an isotropic downward distribution of pitch angles. The condition of no opacity is shown by the solid line, an exit angle of 0° is represented by the dashed line, an exit angle of 80° by the dotted line, and an exit angle of 90° by the dash-dot line. Atmosphere 1 is in black and atmosphere 2 is in gray. Every exit angle is with respect to the Jovian spin axis. The figure on the right is a magnified portion of the figure on the left (represented by the black rectangle), used to emphasize the efficiencies of ions in the energy range of JEDI measurements.

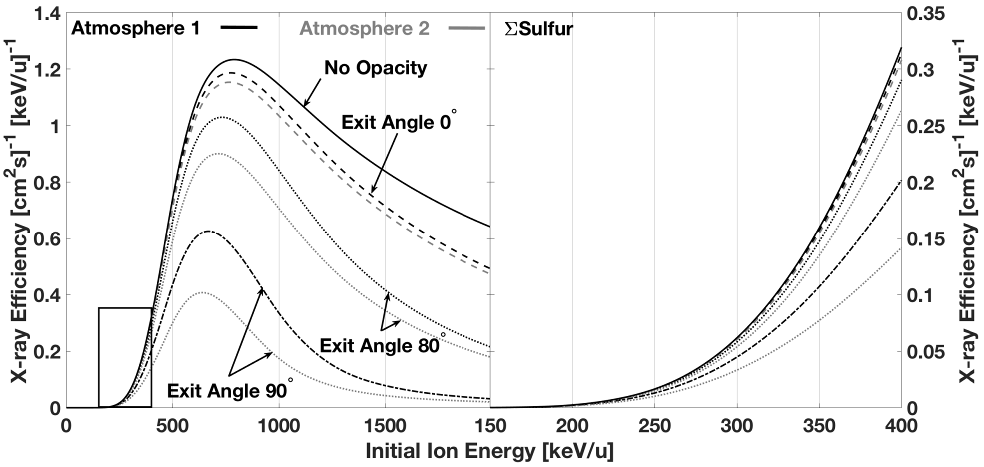

Figure 8. The entire outgoing X-ray flux efficiency for all X-ray producing sulfur charge states as a function of initial ion energy from a single incident ion/cm^2/s with an isotropic downward distribution of pitch angles. The condition of no opacity is shown by the solid line, an exit angle of 0° is represented by the dashed line, an exit angle of 80° by the dotted line, and an exit angle of 90° by the dash-dot line. Atmosphere 1 is in black and atmosphere 2 is in gray. Every exit angle is with respect to the Jovian spin axis. The figure on the right is a magnified portion of the figure on the left (represented by the black rectangle), used to emphasize the efficiencies of ions in the energy range of JEDI measurements.

Ozak et al. (2010) reported that the most efficient X-ray emission for O^{6+}, O^{7+}, and S^{8+} was for incident ions with energies of 1.5 MeV/u, 2.5 MeV/u, and 1 MeV/u, and efficiency values of ∼0.009, ∼0.003, and ∼0.015, respectively. These [c1]energies are 2-3x higher than what JEDI typically observe[c2]s. But our revised model with the SIM cross-sections indicate that for O^{6+}, O^{7+}, and S^{8+} the most efficient X-ray emissions occur at energies of 600 keV/u, 1 MeV/u, and 500 keV/u with efficiencies of 0.29, 0.19, and 0.32, respectively (from Tab. 1, atmosphere 1, 0° viewing angle). Two major contributions account for such a great difference in X-ray efficiencies. First, with the more complete treatment of the fundamental atomic collision processes, it requires much less energy than inferred in the previous models to strip both oxygen and sulfur ions to a high, X-ray producing charge state, allowing X-rays to be created at much lower energies than previously thought. Second, we are depositing much more energy higher up in the atmosphere due to the increase in stopping power shown by Schultz et al. (2019), ultimately generating X-rays higher in the atmosphere than previously modeled, making them less susceptible to opacity effects even when considering an upper-limit, highly-mixed atmosphere.

There are several useful ways to interpret X-ray efficiencies. Because the efficiencies are calculated with an input of 1 ion/cm^2/s, one can view each efficiency as the number of X-ray photons emitted given an initial ion energy. That is to say, if a single oxygen ion with an energy of 300 keV/u is precipitating, then it is expected that ∼0.1 [c1]photons/cm^2/s/(keV/u) x 300 keV/u ≈ 30 photons/cm^2/s will be emitted. Therefore, 1 oxygen ion/cm^2/s at 300 keV/u will produce about 30 photons/cm^2/s, or 1 ion/s precipitating results in 30 photons/s. This is an extremely quick estimate that can be made when trying to interpret the emission from a measured JEDI ion flux and is useful if considering an X-ray instrument for a future mission to Jupiter.

Another practical application of the X-ray efficiencies is to calculate total X-ray power emission for a given initial ion energy. For example; we have just calculated that 1 oxygen ion/s at 300 keV/u will produce 30 photons/s. The average emitted photon energy associated with oxygen is 600 eV (See Section 3.3). The power out is then 30 photons/s x 600 eV x 1.6x10^{-9} [c2]Joules/eV ≈ 3x10^{-15} [c3]Joules/s or 3x10^{-15} Watts. Thus, given an ion flux, one can approximate the total power output from the precipitating ions.

Finally, given an ion flux one can estimate the power output from the entirety of the polar cap, or a defined area that Juno has flown over while an X-ray observation has been made simultaneously. If photons/cm^2/s is calculated, either through the aforementioned method or as a direct result output from our model with a variety of initial ion energies, then finding the power/cm^2/s is a matter of combining the two previous methods. That is, (photons/cm^2/s) x (average photon energy [eV]) x (1.6x10^{-19} [c4]Joules/eV) results in W/cm^2. Now, if the area of the measurement is known, or deduced by geometry, multiplying power/cm^2 by the area will result in the total power for that area, which can be directly compared to an observed total X-ray power (or luminosity).

3.3 X-ray Spectra

Distributing the X-ray intensity into individual lines, as given by the approximate treatment of the synthetic spectra as described in Section 2.5, we can provide X-ray spectra. Figure 9 shows the total X-ray emission for a single oxygen plus a single sulfur ion

[c1] *SJH-1*: ~~required~~
[c2] *SJH-1*: ~~d~~
[c1] *SJH-2*: $\cancel{\frac{\text{photons}}{\text{cm}^2\text{s}}\frac{1}{\text{keV/u}}}$
[c2] *SJH-2*: $\cancel{\frac{\text{Joules}}{\text{eV}}}$
[c3] *SJH-2*: $\cancel{\frac{\text{Joules}}{\text{s}}}$
[c4] *SJH-2*: $\cancel{\frac{\text{Joules}}{\text{eV}}}$

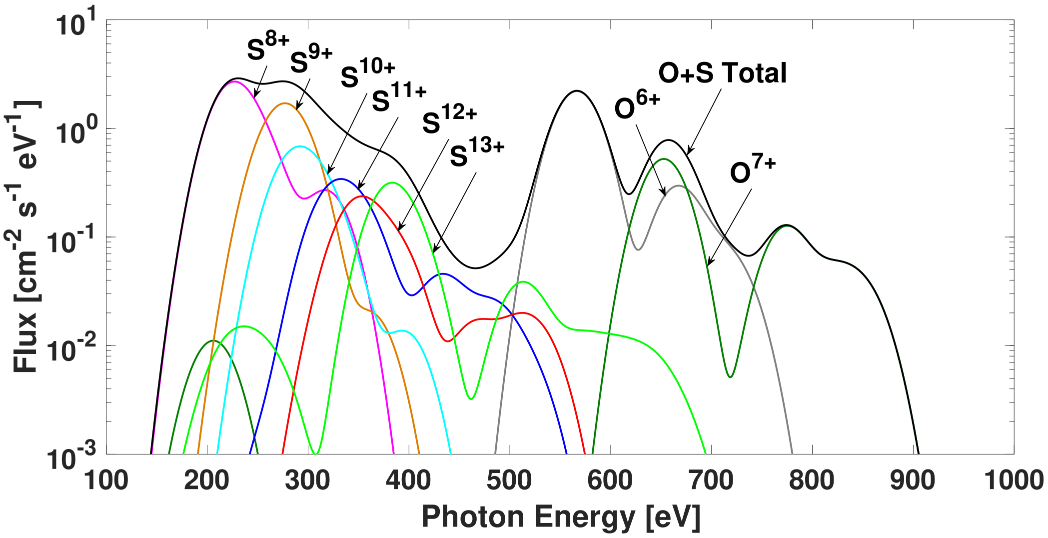

Figure 9. Approximated synthetic X-ray spectra showing the contribution from each charge state. This spectrum includes emission from both charge exchange and direct excitation collisions considering no opacity effects from an incident ion beam of 500 keV/u with an input is 1 ion/cm^2/s for both species. Not shown is the emission from S^{14+} which peaks at $\sim$2450 eV with an intensity several orders of magnitude lower than the more prominent emission lines.

(sulfur to oxygen ratio of 1:1), both with incident energies of 500 keV/u. The emission lines have been distributed with a normalized Gaussian and σ=20 eV, simulating instrument response functions (discussed in Section 2.5). The emission is plotted by charge state to show where in the spectrum each emission line contributes the most, i.e. sulfur dominates at photon energies between 150-500 eV, while oxygen is prominent between 500-900 eV. This particular spectrum (Fig. 9) accounts for no opacity effects and we have included emission from both charge exchange and direct excitation collisions. The emission from S^{14+} has two peaks at $\sim$430 eV and $\sim$2450 eV, but the latter is multiple orders of magnitude below the rest of the emission and would therefore be much fainter than the dominant lines in Figure 9.

Figure 10 is the same total emission from Figure 9 (black line) with opacity effects applied from both atmosphere 1 and 2 at three different viewing angles. It is apparent that [c1]the lower energy X-ray emission[c2]s from sulfur [c3]are much more [c4]affected by opacity than [c5]those from oxygen, which was indicated by the X-ray efficiencies in Table 1. This is due to the relatively large photo-absorption cross-sections at longer wavelengths, shown by Cravens et al. (2006). The relative absorption is useful when comparing emissions from the northern and southern aurorae, because the southern aurora is generally observed at a much steeper viewing angle than the northern aurora.

It is also important to note how little X-ray absorption occurs at this energy of 500 keV/u, even for atmosphere 2. A 500 keV/u oxygen ion (total energy of 8 MeV) is nearing the upper energy limit of the JEDI instrument of 10 MeV (Mauk et al., 2017) and

[c1] *SJH-1*: *Text added.*
[c2] *SJH-1*: *Text added.*
[c3] *SJH-1*: ~~is~~
[c4] *SJH-1*: e
[c5] *SJH-1*: ~~that~~

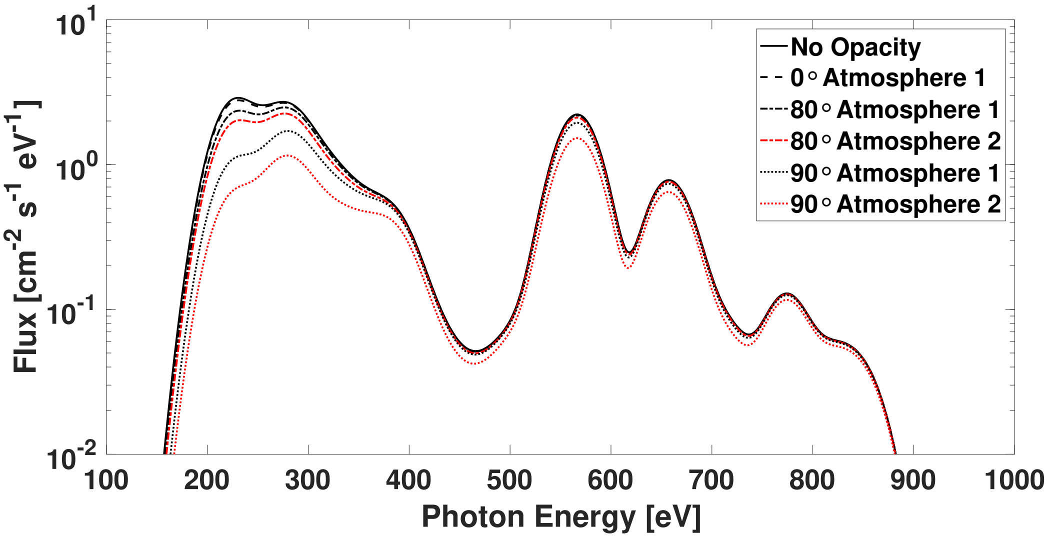

Figure 10. Approximated synthetic X-ray spectra with opacity effects at three viewing angles through an atmosphere with a deep, originally considered homopause (atmosphere 1) and an atmosphere that is well-mixed through the top of the atmosphere (atmosphere 2), what we consider an upper-limit to opacity effects. Initial ion energies are 500 keV/u for both oxygen and sulfur precipitation and the input is 1 ion/cm^2/s for both species. Photon energies below about 400 eV are shown to be much more affected by the opacity than higher photon energies.

a 500 keV/u sulfur ion (16 MeV) is above that limit. This suggests that precipitation of ions with energies within the JEDI limits will have X-ray emission that will escape without undergoing large opacity effects, and should be detectable, even if a very well-mixed atmosphere is present. Due to the new SIM cross-sections precluding the X-ray producing ions [c6]from precipitat[c7]ing deep into the atmosphere, these results are much different than those presented by Ozak et al. (2010), which show a reduction in sulfur emission by nearly two orders of magnitude when considering a 90° viewing angle.

3.4 Inputting JEDI Measurements

Finally, we input the JEDI flux measurements, displayed in Figure 4, into our model and are able to determine ion production rates, direct excitation rates, and an expected X-ray spectrum. In the results presented using JEDI measurements we only consider atmosphere 1, the original atmosphere in Figure 1 with a well defined homopause. Displayed in Figure 11 are the ion production rates from X-ray producing charge exchange collisions (TI, SC, SC+SS) combined with the production rates from X-ray producing direct excitation collisions (SI+SPEX, DI+SPEX, and TEX+SPEX) associated with the PJ 7 ion flux measurements. This demonstrates that the ions seen during this pass are of sufficient energy to reach X-ray producing charge states. It is also evident that X-ray emitting ions do not precipitate deeply enough to go much below the homopause, indicating that absorption will have minimal effects.

[c6] *SJH-1*: ~~to~~
[c7] *SJH-1*: ~~e~~

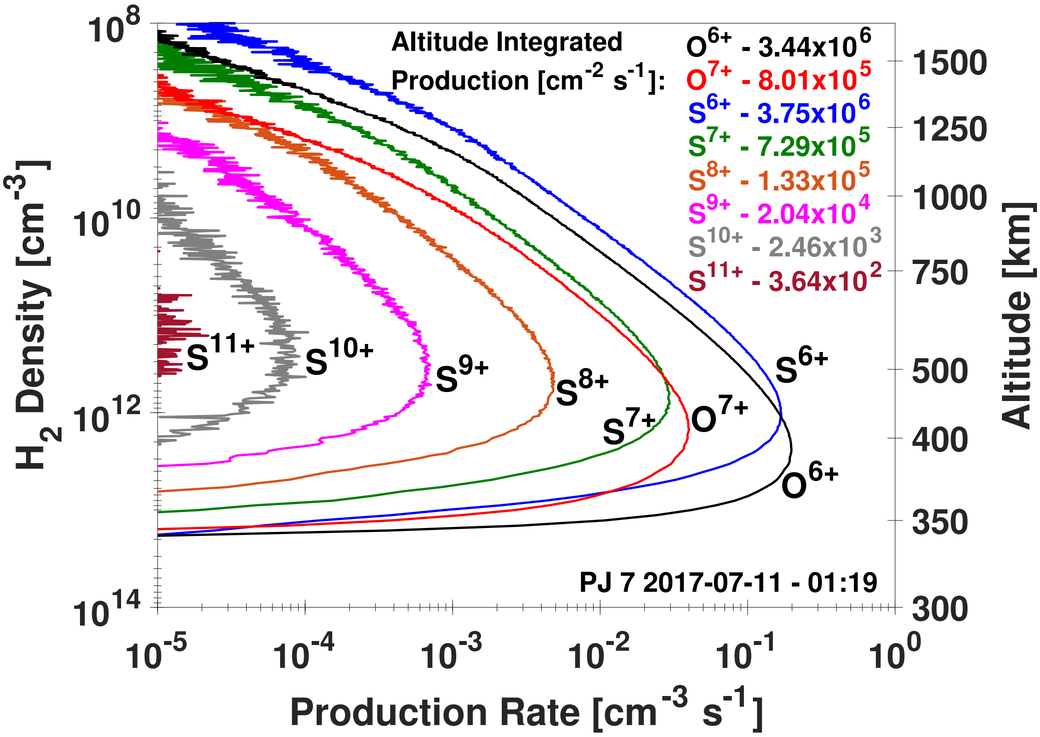

Figure 11. Ion production rate from X-ray producing charge exchange collisions combined with X-ray producing direct excitation collisions of each ion charge state vs. H_2 density and altitude from Juno's PJ 7 pass. Also included is the altitude integrated production rate of each charge state displayed. It is evident from the charge states obtained that X-rays will be produced.

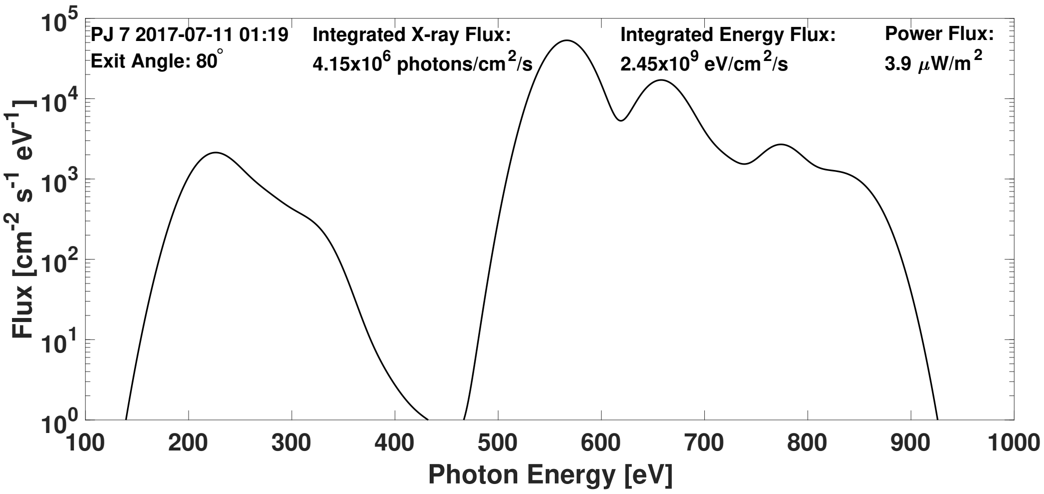

Figure 12. Predicted X-ray spectrum from JEDI's ion flux measurements during the PJ 7 polar cap pass in 2017. This spectrum assumes an opacity effect with an exit angle of 80° through atmosphere 1. It appears emission from oxygen is the most prominent source of X-rays associated with this flux measurement, which may have been anticipated from the JEDI data taken at this time, but is likely not always the case.

Displayed in [c1]Figure 12 is the X-ray spectrum we predict using [c2]a JEDI[c3] measurement [c4]of an instant of a particularly high ion flux during PJ 7 (Fig. 4), included is X-ray production from both charge exchange and direct excitation collisions. This particular spectrum considers opacity effects with a photon exit angle of 80°, which we assume to be a common viewing angle from earth-orbit-based observations; although, opacity effects make little difference on the X-ray emission from ions with this low of initial energy. (When comparing an 80° exit angle to a 90° exit angle, the total emitted flux from oxygen emission was only reduced by 5.4% for the 90° case, while emission from sulfur was diminished by 15%.)

3.5 Comparing Simulated and Observed X-ray Spectra

The XMM-Newton Observatory observed Jupiter continuously from 19:29 on July 10th to 09:38 on July 12th, 2017. Part of this observation was simultaneous with the Juno JEDI ion measurements presented in Section 3.4 and Figure 4. Unfortunately, since Jupiter's aurorae rotate with the planet, the Northern X-ray aurora was not in view from Earth precisely when Juno conducted *in situ* particle measurements in the X-ray auroral region, but was observable two hours prior to this and one hour after (see supporting information for comparisons of Juno flight with auroral viewing). Here, we compare the simulated Northern auroral X-ray spectrum from the Juno JEDI *in situ* measurements with contemporaneous observed X-ray auroral spectrum.

We extracted and calibrated the observed X-ray spectrum from Jupiter's Northern aurora during the two intervals (19:29-21:30 on July 10th and 01:00-06:00 on July

[c1] *SJH-1*: ~~f~~
[c2] *SJH-1*: *Text added.*
[c3] *SJH-1*: ~~'s measured ion flux~~
[c4] *SJH-1*: *Text added.*

11th (UT)) that bracketed the Juno JEDI ion measurements (Sec. 3.4; Fig. 4 & Fig. 12). [c1]One-way light travel from Jupiter to XMM-Newton between July 10th - 12th, 2017 was 45 minutes. The northern aurora rotated out of view for XMM-Newton at ∼21:30 UT (light emitted from Jupiter at 20:45) and came back into view at ∼01:50 (light emitted from Jupiter at 01:05). During this interval there was not perfect coincidence of Juno measuring the X-ray emitting region and the subsequent X-rays being observed at Earth. We found that the X-ray aurora in this interval was relatively dim (∼50% of the power output observed in the subsequent two auroral observations on the July 11 and July 12 supporting information).

We took the simulated X-ray photon fluxes emitted from the *in situ* ion flux measurements at a 60 degree viewing angle, to represent the latitudinal location of the observed [c1]northern X-ray emissions (e.g. see Gladstone et al. (2002); Dunn et al. (2017)). We multiplied these photon fluxes per cm^2 by the area of a typical dim X-ray auroral region (e.g. time-binned X-ray projections in Dunn et al. (2016)) to attain a total flux of photons from the aurora. We then scaled these auroral photon fluxes by [c2]$4\pi r^2$ to account for their dispersion between Jupiter and XMM-Newton. Having calculated fluxes arriving at XMM, we applied XMM-Newton's time-dependent instrument responses on July 10th (XMM-Newton calibration, response matrices, and ancillary response files) to the simulated photon fluxes. This provided a simulated X-ray spectrum for what would be detected by XMM-Newton on July 10-11th, 2017. Finally, we compared the simulated and observed spectra by calculating the reduced Chi-Squared between the two.

Figure 13 shows the comparison between the simulated spectrum (black lines) and the observed data from 19:29-21:30 on July 10th, 2017 (blue crosses). The results were similar for both intervals (see supporting information). The simulated oxygen emission between 0.5-0.9 keV is an excellent fit to the observed spectrum for both intervals producing a reduced χ^2 of 1.3-1.5 (Table 12). However, below 0.5 keV the simulated sulfur photon fluxes do not well reproduce the observed emission, which leads to a reduced χ^2 of 4-5 for the overall spectrum from both intervals (Table 12). Consequently, we investigate a "boosted" sulfur model (black dash-dotted line in Fig. 13) to determine how much sulfur emission is necessary to reproduce the observed spectrum. A sulfur boost of 100x is needed to fit the emission measured by XMM-Newton; this is concerning due to the luminosity associated with this large of a boost (∼7 GW[c11], which is notably higher than typical X-ray observations, discussed in Section 3.6). This lower energy spectrum could also be fit well with a bremsstrahlung continuum, but this does not resolve the high luminosity issue. Alternatively, this discrepancy may be a result of the poor effective area for the XMM-Newton EPIC-pn instrument below 0.3 keV. Ultimately, more input data (JEDI measurements) and XMM-Newton observation comparisons are required for greater statistical significance; because, as Figure 4 indicates, the high energy tail of the sulfur spectrum falls off more rapidly than that of oxygen, which is likely not always the case. [c12]It is to be considered that the sulfur data is preliminary; however, we do not expect any substantial changes in the sulfur cross-sections to resolve the disagreement presented here.

The spectral morphology in [c13]the <0.3 keV X-ray energy range appears line-like, but could also be fitted well by a large flux of photons from a low energy bremsstrahlung continuum (see supporting information for details). The discrepancy between 0.2-0.5[c14]

[c1] *SJH-1*: *Text added.*
[c1] *SJH*: ~~N~~
[c2] *SJH-1*: ~~2~~
[c11] *SJH-2*: *Text added.*
[c12] *SJH-2*: *Text added.*
[c13] *SJH-1*: ~~this~~
[c14] *SJH-1*: *Text added.*

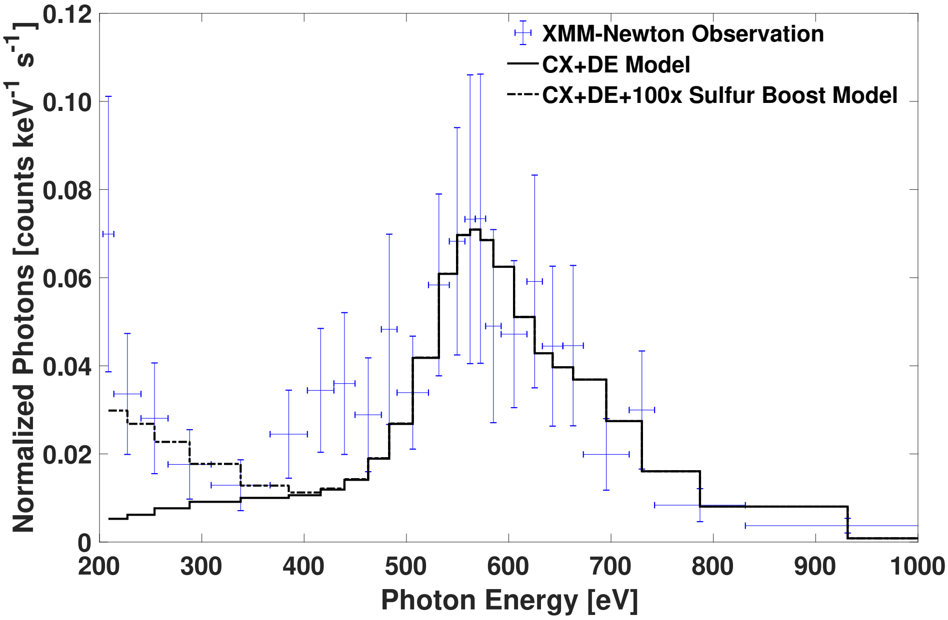

Figure 13. An XMM-Newton EPIC-pn observation of Jupiter's Northern X-ray Auroral spectrum from 19:29-21:30 on July 10th, 2017 (blue crosses) binned to ensure at least 5 counts per energy channel. Overlaid on the observational data is the simulated photon fluxes from Figure 12 [c7]that has been normalized using the XMM-Newton EPIC-pn instrument response to produce a simulated X-ray spectrum (black solid line, S:O ratio of 0.8) and a second, sulfur boost of 100x, X-ray spectrum (black dash-dotted line). This assumes an X-ray auroral region of [c8]2.5° x 7.5° [c9](a surface area of ∼2x10^{17} cm^2) System III latitude-longitude[c10], demonstrating a good morphological fit to the spectra based on the shape of emission.

keV also appears between Figures 10 and 12. Figure 4 shows that there was an S:O ratio of 0.8 during this interval. Radioti et al. (2005, 2006) showed that the S:O ratio in the magnetosphere varies from 0.3-1.2, so this ratio appears to be a typical measurement. However, figures 9 and 10 suggest that this may have been an intermittent relatively low ratio, showing that an S:O ratio of 1:1 [c15]produces a spectrum that morphologically is much closer to the observed X-ray spectrum. Thus, a secondary process (aside from sulfur precipitation) should likely be considered to contribute to that part of the spectrum. The X-ray aurora is also known to be highly time variable on scales of 10s of minutes to hours (e.g. Dunn et al. (2017)) so it may be that the conditions changed between the perijove pass through the X-ray auroral zone and the auroral emissions that were observed.

To account for the low predicted sulfur emission, we [c1]briefly consider a bremsstrahlung component to either replicate a forest of sulfur lines between 0.2-0.5 keV or to reproduce a high energy bremsstrahlung component (above 0.9 keV), which is sometimes present in the X-ray aurora from energetic electrons (e.g. Branduardi-Raymont et al. (2004, 2008)).

[c15] *SJH*: ~~ratio~~
[c1] *SJH*: *Text added.*

Observation Time	Model	Reduced χ^2 Fits	Auroral Power Observed [mW/m^2]	Auroral Power Simulated [mW/m^2]
10 July 19:29-21:30	CX+DE	5	1x10^{-13}	3x10^{-14}
10 July 19:29-21:30	CX+DE+ Bremsstrahlung	1.3	1x10^{-13}	7x10^{-14}
11 July 01:00-05:30	CX+DE	4	8x10^{-14}	3x10^{-14}
11 July 01:00-05:30	CX+DE+ Bremsstrahlung	1.5	8x10^{-14}	5x10^{-14}

Table 2. Table showing XMM-Newton Northern auroral observations with auroral models, their resulting reduced χ^2 fits and the observed and simulated auroral powers.

Including these bremsstrahlung components was found to improve the fits (Table 12)[c2]. Much of Jupiter's UV aurora is known to be produced by electron precipitation and a bremmstrahlung continuum has been found to provide an excellent fit to the X-ray emission above 2 keV in Branduardi-Raymont et al. (2004)[c3]. But, in this work we concentrate on the spectral line emission from ion precipitation. Figures for these fits can be found in the supporting information alongside comparisons of the Juno flight path with the X-ray auroral emission region and X-ray lightcurves from this interval.

In summary, our models produce excellent predictions for the observed X-ray emission from oxygen precipitation into the atmosphere, if the X-ray auroral zone covers a region of between 5° to 10° by 5° to 10° in System III latitude-longitude. There are still open questions about whether the sulfur emission is under-estimated because of time-varying changes in the ion precipitation or because of some, as yet unidentified, differences between the treatment of oxygen and sulfur behaviour. To identify this will require additional XMM-Newton observations coincident with Juno measurements at perijove. These observations are planned for September 2019.

3.6 X-ray Luminosity

Can heavy ion precipitation produce *enough* X-ray emission to explain the total observational soft X-ray luminosity of 1-2 GW (Elsner et al., 2005; Gladstone et al., 2002) A quick estimate confirms that the new model can produce such luminosity. The X-ray emission our model produces when the JEDI ion flux measurement shown in Figure 4 are input is ~4x10^6 photons/cm^2/s. This is the sum of all oxygen and sulfur X-ray emission from both charge exchange and direct excitation with an exit angle of 80° from the original atmosphere. Integrating the emission in Figure 12[c1], results in ~2.5x10^9 eV/cm^2/s. Converting this to Watts/cm^2 by multiplying by a factor of 1.6x10^{-19} J/eV yields a power output of 4x10^{-9} W/cm^2. Now, the total area of X-ray emission on the Jovian polar cap can be assumed to come from within a latitude of ~5°. This gives an area of $2\pi R_J^2(1-\cos\theta) \approx 10^{18}$ cm^2 (R_J = Jovian radii = 71,492 km). 4x10^{-9} W/cm^2 x 10^{18} cm^2 = 4x10^9 W, or 4 GW. It appears, based on this quick, "back of the envelope" calculation, that we can now account for the entirety of the output power of the X-rays. Of course, the area of emission needs to be greatly constrained[c2] and this was for a single, instanta-

[c2] *SJH-1*: ~~; however, no physical explanation (i.e. electron flux measurements) for the electron bremsstrahlung is provided here.~~
[c3] *SJH-1*: *Text added.*
[c1] *SJH-1*: Changed
[c2] *SJH-1*: *Text added.*

neous JEDI measurement that observed a high ion flux, but this shows it is now feasible the ion flux measurements at Jupiter are responsible for the X-ray emission.

4 Discussion and Conclusions

Spectral lines from precipitating ions have been known to dominate Jupiter's X-ray aurora since the launch of XMM-Newton and Chandra in 1999 (Branduardi-Raymont et al., 2004; Elsner et al., 2005). New *in situ* measurements by Juno have detected the ion precipitation that leads to these X-ray emissions. Previous modeling required much higher energy ions (Cravens et al., 1995; Ozak et al., 2010, 2013; Houston et al., 2018), which were difficult to explain with given knowledge of Jupiter's magnetosphere. This forced us to rethink the processes producing X-ray emission from ion precipitation. Schultz et al. (2019) determined not every process was being accounted for in the original precipitation modeling, but simultaneous processes (both target and ion) needed to be considered. This led to a completely new series of processes and cross-sections that we have now utilized for the updated heavy ion precipitation model described here. The initial ion energy necessary to produce X-rays has been reduced dramatically, and is now well within the heavy ion energy range being measured by the Juno spacecraft.

To summarize the findings of our model:

1. New data, accounting for SIM processes has shifted the charge state distribution of both oxygen and sulfur to lower energies than before. The repercussions being it now requires less energy to strip ions to X-ray producing charge states, resulting in precipitation that does not penetrate as deeply into the atmosphere.
2. Direct excitation is now considered as a new X-ray production mechanism, which adds to the total flux and to the spectrum.
3. Because the ions are not precipitating as deep into the atmosphere as previous models suggested, there is less absorption of photon emission when opacity effects are considered.
4. If an atmosphere of fully mixed constituents is used, the X-ray efficiency is reduced; but, emission from ions at the energies measured by JEDI is only reduced by about 15-20% compared to the original atmosphere.
5. While the oxygen collisional data have been carefully checked and published, the analogous data for sulfur utilized here in a preliminary form is now in final preparation and checking for publication.
6. X-ray spectra separated into line emission using Gaussian distributions are producible and can be used in coordination with JEDI ion flux measurements and earth-orbit-based X-ray observations. When comparing the two, opacity effects need to be considered based on the geometry of the earth and Jupiter at the time.
7. Approximated synthetic X-ray spectra comparisons with XMM-Newton observations have good agreement with oxygen emission; however, lower energy photoemission needs to be explored further to isolate the discrepancy at lower energies, in the sulfur part of the spectrum. This could be by having an increased sulfur flux or by including emission from electron bremsstrahlung. [c1]Although the sulfur data is preliminary, we do not expect any changes to the data to be significant enough to resolve the differences seen.
8. JEDI flux measurements input into the model generate enough X-rays to account for the total X-ray power that has been observed in the past.

This paper has shown that the observed soft X-ray auroral emission from Jupiter can indeed be explained by the precipitation of energy heavy ions (as observed by Juno).

[c1] *SJH-2: Text added.*

Hence, X-ray observation can be used to estimate heavy ion fluxes with energies in excess of ∼200 keV/u (i.e., 3 MeV and higher) and to determine the morphology of this precipitation made over the polar caps. Such precipitation has been shown to be associated with downward field-aligned currents, both due to the primary ion precipitation and the resultant secondary electron escape from the atmosphere (Cravens et al., 2003; Houston et al., 2018; Ozak et al., 2010, 2013). The ion precipitation is also responsible as a source of ionization in the thermosphere, [c2]which was explored further in the earlier model presented by Houston et al. (2018). [c3]The model established here has very similar atmospheric ion production rates as previously reported. But a deeper discussion is reserved for a future publication, to examine the affects on ionospheric conductivities, which are important for understanding magnetosphere-ionosphere coupling. Much work remains to be done on the Jovian polar aurora.

[c2] *SJH-2*: *Text added.*

[c3] *SJH-2*: ~~and here will affect~~

Acknowledgments

This work was supported at the University of Kansas by NASA grant NNX14AG79G. See the supporting information for data used to produce the figures and tables in this paper. [c1]Data associated with the ion precipitation model used here can be found on the corresponding AGU website and all X-ray data presented here are publicly available on the XMM-Newton Science archive: https://nxsa.esac.esa.int/nxsa-web/#search.

References

Branduardi-Raymont, G., Bhardwaj, A., Elsner, R. F., Gladstone, G. R., Ramsay, G., Rodriguez, P., … Cravens, T. E. (2007). A study of Jupiter's aurorae with XMM-Newton. *A & A*, *463*(2), 761-774. Retrieved from https://doi.org/10.1051/0004-6361:20066406 doi: 10.1051/0004-6361:20066406

Branduardi-Raymont, G., Elsner, R. F., Galand, M., Grodent, D., Cravens, T. E., Ford, P., … Waite, J. H. (2008). Spectral morphology of the X-ray emission from Jupiter's aurorae. *Journal of Geophysical Research: Space Physics*, *113*(A2). Retrieved from http://dx.doi.org/10.1029/2007JA012600 (A02202) doi: 10.1029/2007JA012600

Branduardi-Raymont, G., Elsner, R. F., Gladstone, G. R., Ramsay, G., Rodriguez, P., Soria, R., & Waite, J. H. (2004). First observation of Jupiter by XMM-Newton. *A&A*, *424*(1), 331-337. Retrieved from https://doi.org/10.1051/0004-6361:20041149 doi: 10.1051/0004-6361:20041149

Clark, G., Mauk, B. H., Haggerty, D., Paranicas, C., Kollmann, P., Rymer, A., … Valek, P. (2017, September). Energetic particle signatures of magnetic field-aligned potentials over Jupiter's polar regions. *grl*, *44*, 8703-8711. doi: 10.1002/2017GL074366

Clark, G., Mauk, B. H., Paranicas, C., Haggerty, D., Kollmann, P., Rymer, A., … Valek, P. (2017, May). Observation and interpretation of energetic ion conics in Jupiter's polar magnetosphere. *grl*, *44*, 4419-4425. doi: 10.1002/2016GL072325

Clark, G., Tao, C., Mauk, B. H., Nichols, J., Saur, J., Bunce, E. J., … Valek, P. (2018). Precipitating electron energy flux and characteristic energies in Jupiter's main auroral region as measured by Juno/JEDI. *Journal of Geophysical Research: Space Physics*, *123*(9), 7554-7567. Retrieved from https://agupubs.onlinelibrary.wiley.com/doi/abs/10.1029/2018JA025639 doi: 10.1029/2018JA025639

Connerney, J. E. P., Adriani, A., Allegrini, F., Bagenal, F., Bolton, S. J., Bonfond, B., … Waite, J. (2017). Jupiter's magnetosphere and aurorae observed by the Juno spacecraft during its first polar orbits. *Science*, *356*(6340), 826–832. Retrieved from http://science.sciencemag.org/content/356/6340/826 doi: 10.1126/science.aam5928

Connerney, J. E. P., Kotsiaros, S., Oliversen, R. J., Espley, J. R., Joergensen, J. L., Joergensen, P. S., … Levin, S. M. (2018). A new model of Jupiter's magnetic field from Juno's first nine orbits. *Geophysical Research Letters*, *45*(6), 2590-2596. Retrieved from https://agupubs.onlinelibrary.wiley.com/doi/abs/10.1002/2018GL077312 doi: 10.1002/2018GL077312

Cravens, T. E., Clark, J., Bhardwaj, A., Elsner, R., Waite Jr., J. H., Maurellis, A. N., … Branduardi-Raymont, G. (2006). X-ray emission from the outer planets: Albedo for scattering and fluorescence of solar X rays. *Journal of Geophysical Research: Space Physics*, *111*(A7). Retrieved from https://agupubs.onlinelibrary.wiley.com/doi/abs/10.1029/2005JA011413 doi: 10.1029/2005JA011413

[c1] *SJH-2: Text added.*

Cravens, T. E., Howell, E., Waite, J. H., & Gladstone, G. R. (1995). Auroral oxygen precipitation at Jupiter. *Journal of Geophysical Research: Space Physics*, *100*(A9), 17153-17161. Retrieved from https://agupubs.onlinelibrary.wiley.com/doi/abs/10.1029/95JA00970 doi: 10.1029/95JA00970

Cravens, T. E., Waite, J. H., Gombosi, T. I., Lugaz, N., Gladstone, G. R., Mauk, B. H., & MacDowall, R. J. (2003). Implications of Jovian X-ray emission for magnetosphere-ionosphere coupling. *Journal of Geophysical Research: Space Physics*, *108*(A12). Retrieved from http://dx.doi.org/10.1029/2003JA010050 (1465) doi: 10.1029/2003JA010050

Delamere, P. A., Bagenal, F., & Steffl, A. (2005). Radial variations in the Io plasma torus during the Cassini era. *Journal of Geophysical Research: Space Physics*, *110*(A12). Retrieved from https://agupubs.onlinelibrary.wiley.com/doi/abs/10.1029/2005JA011251 doi: 10.1029/2005JA011251

Dougherty, L. P., Bodisch, K. M., & Bagenal, F. (2017). Survey of Voyager plasma science ions at Jupiter: 2. Heavy ions. *Journal of Geophysical Research: Space Physics*, *122*(8), 8257-8276. Retrieved from https://agupubs.onlinelibrary.wiley.com/doi/abs/10.1002/2017JA024053 doi: 10.1002/2017JA024053

Dunn, W. R., Branduardi-Raymont, G., Elsner, R. F., Vogt, M. F., Lamy, L., Ford, P. G., … Jasinski, J. M. (2016). The impact of an icme on the Jovian X-ray aurora. *Journal of Geophysical Research: Space Physics*, *121*(3), 2274-2307. Retrieved from https://agupubs.onlinelibrary.wiley.com/doi/abs/10.1002/2015JA021888 doi: 10.1002/2015JA021888

Dunn, W. R., Branduardi-Raymont, G., Ray, L. C., Jackman, C. M., Kraft, R. P., Elsner, R. F., … Coates, A. J. (2017). The independent pulsations of Jupiter's northern and southern X-ray auroras. *Nature Astronomy*, *1*(11), 758–764. Retrieved from https://doi.org/10.1038/s41550-017-0262-6 doi: 10.1038/s41550-017-0262-6

Elsner, R. F., Lugaz, N., Waite, J. H., Cravens, T. E., Gladstone, G. R., Ford, P., … Majeed, T. (2005). Simultaneous Chandra X-ray, Hubble Space Telescope ultraviolet, and Ulysses radio observations of Jupiter's aurora. *Journal of Geophysical Research: Space Physics*, *110*(A1). Retrieved from http://dx.doi.org/10.1029/2004JA010717 (A01207) doi: 10.1029/2004JA010717

Folkner, W. M., Iess, L., Anderson, J. D., Asmar, S. W., Buccino, D. R., Durante, D., … Levin, S. M. (2017). Jupiter gravity field estimated from the first two Juno orbits. *Geophysical Research Letters*, *44*(10), 4694-4700. Retrieved from https://agupubs.onlinelibrary.wiley.com/doi/abs/10.1002/2017GL073140 doi: 10.1002/2017GL073140

Gérard, J.-C., Bonfond, B., Grodent, D., Radioti, A., Clarke, J. T., Gladstone, G. R., … Shematovich, V. I. (2014). Mapping the electron energy in Jupiter's aurora: Hubble spectral observations. *Journal of Geophysical Research: Space Physics*, *119*(11), 9072–9088. Retrieved from http://dx.doi.org/10.1002/2014JA020514 (2014JA020514) doi: 10.1002/2014JA020514

Gladstone, G. R., Waite, J. H., Grodent, D., Lewis, W. S., Crary, F. J., Elsner, R. F., … Cravens, T. E. (2002, 02 28). A pulsating auroral X-ray hot spot on Jupiter. *Nature*, *415*(6875), 1000–1003. Retrieved from http://dx.doi.org/10.1038/4151000a

Grozdanov, T., & Janev, R. (1978). One-electron capture in slow collisions of highly charged ions with atoms. *Physics Letters A*, *66*(3), 191 - 194. Retrieved from http://www.sciencedirect.com/science/article/pii/0375960178906539 doi: https://doi.org/10.1016/0375-9601(78)90653-9

Haggerty, D. K., Mauk, B. H., Paranicas, C. P., Clark, G., Kollmann, P., Rymer, A. M., … Levin, S. M. (2017). Juno/JEDI observations of 0.01 to >10 MeV energetic ions in the Jovian auroral regions: Anticipating a source for polar X-ray emission. *Geophysical Research Letters*, *44*(13), 6476–6482. Retrieved from http://dx.doi.org/10.1002/2017GL072866 (2017GL072866) doi:

10.1002/2017GL072866

Houston, S. J., Ozak, N., Young, J., Cravens, T. E., & Schultz, D. R. (2018). Jovian auroral ion precipitation: Field-aligned currents and ultraviolet emissions. *Journal of Geophysical Research: Space Physics*, *123*(3), 2257-2273. Retrieved from https://agupubs.onlinelibrary.wiley.com/doi/abs/10.1002/2017JA024872 doi: 10.1002/2017JA024872

Hui, Y., Schultz, D. R., Kharchenko, V. A., Bhardwaj, A., Branduardi-Raymont, G., Stancil, P. C., ... Dalgarno, A. (2010). Comparative analysis and variability of the Jovian X-ray spectra detected by the Chandra and XMM-Newton observatories. *Journal of Geophysical Research: Space Physics*, *115*(A7). Retrieved from https://agupubs.onlinelibrary.wiley.com/doi/abs/10.1029/2009JA014854 doi: 10.1029/2009JA014854

Iess, L., Folkner, W. M., Durante, D., Parisi, M., Kaspi, Y., Galanti, E., ... Bolton, S. J. (2018, 03 07). Measurement of Jupiter's asymmetric gravity field. *Nature*, *555*, 220 EP -. Retrieved from https://doi.org/10.1038/nature25776

Jackman, C., Knigge, C., Altamirano, D., Gladstone, R., Dunn, W., Elsner, R., ... Ford, P. (2018). Assessing quasi-periodicities in Jovian X-ray emissions: Techniques and heritage survey. *Journal of Geophysical Research: Space Physics*, *123*(11), 9204–9221.

Kim, T. K., Ebert, R., Valek, P., Allegrini, F., McComas, D., Bagenal, F., ... Nicolaou, G. (2019). Method to derive ion properties from Juno JADE including abundance estimates for O^+ and S^{2+}. *Journal of Geophysical Research: Space Physics*, *0*. Retrieved from https://agupubs.onlinelibrary.wiley.com/doi/abs/10.1029/2018JA026169 doi: 10.1029/2018JA026169

Mauk, B. H., Haggerty, D. K., Jaskulek, S. E., Schlemm, C. E., Brown, L. E., Cooper, S. A., ... Stokes, M. R. (2017, Nov 01). The Jupiter Energetic Particle Detector Instrument (JEDI) investigation for the Juno mission. *Space Science Reviews*, *213*(1), 289–346. Retrieved from https://doi.org/10.1007/s11214-013-0025-3 doi: 10.1007/s11214-013-0025-3

Maurellis, A. N., & Cravens, T. E. (2001). Ionospheric effects of comet Shoemaker-Levy 9 impacts with Jupiter. *Icarus*, *154*(2), 350 - 371. Retrieved from http://www.sciencedirect.com/science/article/pii/S0019103501967090 doi: https://doi.org/10.1006/icar.2001.6709

Metzger, A. E., Luthey, J. L., Gilman, D. A., Hurley, K. C., Schnopper, H. W., Seward, F. D., & Sullivan, J. D. (1983, October). The detection of x rays from Jupiter. *Journal of Geophysical Research*, *88*, 7731-7741. doi: 10.1029/JA088iA10p07731

Moore, K. M., Yadav, R. K., Kulowski, L., Cao, H., Bloxham, J., Connerney, J. E. P., ... Levin, S. M. (2018). A complex dynamo inferred from the hemispheric dichotomy of Jupiter's magnetic field. *Nature*, *561*(7721), 76–78. Retrieved from https://doi.org/10.1038/s41586-018-0468-5 doi: 10.1038/s41586-018-0468-5

Olson, R. E. (1981, Oct). n,l distributions in A^{q+} + H electron-capture collisions. *Phys. Rev. A*, *24*, 1726–1733. Retrieved from https://link.aps.org/doi/10.1103/PhysRevA.24.1726 doi: 10.1103/PhysRevA.24.1726

Oppenheimer, J. R. (1928, Mar). On the quantum theory of the capture of electrons. *Phys. Rev.*, *31*, 349–356. Retrieved from https://link.aps.org/doi/10.1103/PhysRev.31.349 doi: 10.1103/PhysRev.31.349

Orton, G. S., Hansen, C., Caplinger, M., Ravine, M., Atreya, S., Ingersoll, A. P., ... Bolton, S. (2017). The first close-up images of Jupiter's polar regions: Results from the juno mission junocam instrument. *Geophysical Research Letters*, *44*(10), 4599-4606. Retrieved from https://agupubs.onlinelibrary.wiley.com/doi/abs/10.1002/2016GL072443 doi: 10.1002/2016GL072443

Ozak, N., Cravens, T. E., & Schultz, D. R. (2013). Auroral ion precipitation at Jupiter: Predictions for Juno. *Geophysical Research Letters*, *40*(16), 4144–4148. Retrieved from http://dx.doi.org/10.1002/grl.50812 doi: 10.1002/grl.50812

Ozak, N., Schultz, D. R., Cravens, T. E., Kharchenko, V., & Hui, Y.-W. (2010). Auroral X-ray emission at Jupiter: Depth effects. *Journal of Geophysical Research: Space Physics*, *115*(A11). Retrieved from http://dx.doi.org/10.1029/2010JA015635 (A11306) doi: 10.1029/2010JA015635

Parkinson, C. D., Stewart, A. I. F., Wong, A. S., Yung, Y. L., & Ajello, J. M. (2006). Enhanced transport in the polar mesosphere of Jupiter: Evidence from Cassini UVIS helium 584 Å airglow. *Journal of Geophysical Research: Planets*, *111*(E2). Retrieved from https://agupubs.onlinelibrary.wiley.com/doi/abs/10.1029/2005JE002539 doi: 10.1029/2005JE002539

Radioti, A., Krupp, N., Woch, J., Lagg, A., Glassmeier, K.-H., & Waldrop, L. S. (2005). Ion abundance ratios in the Jovian magnetosphere. *Journal of Geophysical Research: Space Physics*, *110*(A7). Retrieved from https://agupubs.onlinelibrary.wiley.com/doi/abs/10.1029/2004JA010775 doi: 10.1029/2004JA010775

Radioti, A., Krupp, N., Woch, J., Lagg, A., Glassmeier, K.-H., & Waldrop, L. S. (2006). Correction to “Ion abundance ratios in the Jovian magnetosphere”. *Journal of Geophysical Research: Space Physics*, *111*(A10). Retrieved from https://agupubs.onlinelibrary.wiley.com/doi/abs/10.1029/2006JA011990 doi: 10.1029/2006JA011990

Sada, P., Bjoraker, G., Jennings, D., McCabe, G., & Romani, P. (1998, December). Observations of CH4, C2H6, and C2H2 in the stratosphere of Jupiter. *Icarus*, *136*(2), 192201. Retrieved from https://doi.org/10.1006/icar.1998.6021 doi: 10.1006/icar.1998.6021

Sánchez-Lavega, A., Hueso, R., Eichstädt, G., Orton, G., Rogers, J., Hansen, C. J., … Bolton, S. (2018, October). The Rich Dynamics of Jupiter's Great Red Spot from JunoCam: Juno Images. *Astronomical Journal*, *156*, 162. doi: 10.3847/1538-3881/aada81

Schultz, D. R., Gharibnejad, H., Cravens, T. E., & Houston, S. J. (2019). Data for secondary-electron production from ion precipitation at Jupiter ii: Simultaneous and non-simultaneous target and projectile processes in collisions of oq+ + h2 (q=0...8). *Atomic Data and Nuclear Data Tables*, *126*, 1 - 69. Retrieved from http://www.sciencedirect.com/science/article/pii/S0092640X18300627 doi: https://doi.org/10.1016/j.adt.2018.08.002

Schultz, D. R., Lee, T.-G., & Loch, S. D. (2010, jul). Calculations and analysis of cross sections required for argon charge exchange recombination spectroscopy. *Journal of Physics B: Atomic, Molecular and Optical Physics*, *43*(14), 144002. Retrieved from https://doi.org/10.1088%2F0953-4075%2F43%2F14%2F144002 doi: 10.1088/0953-4075/43/14/144002

Schultz, D. R., Ozak, N., Cravens, T. E., & Gharibnejad, H. (2017). Ionization of molecular hydrogen and stripping of oxygen atoms and ions in collisions of $O^{q+} + H_2$ (q = 0 - 8): Data for secondary electron production from ion precipitation at Jupiter. *Atomic Data and Nuclear Data Tables*, *113*, 1 - 116. Retrieved from http://www.sciencedirect.com/science/article/pii/S0092640X16300109 doi: 10.1016/j.adt.2016.04.003

Seiff, A., Kirk, D. B., Knight, T. C. D., Mihalov, J. D., Blanchard, R. C., Young, R. E., … Wang, J. (1996). Structure of the atmosphere of Jupiter: Galileo probe measurements. *Science*, *272*(5263), 844–845. Retrieved from http://science.sciencemag.org/content/272/5263/844 doi: 10.1126/science.272.5263.844

Seiff, A., Kirk, D. B., Knight, T. C. D., Young, L. A., Milos, F. S., Venkatapathy, E., … Schubert, G. (1997). Thermal structure of Jupiter's upper atmosphere derived from the Galileo probe. *Science*, *276*(5309), 102–104. Retrieved from http://science.sciencemag.org/content/276/5309/102 doi:

10.1126/science.276.5309.102

Sinclair, J., Orton, G., Greathouse, T., Fletcher, L., Moses, J., Hue, V., & Irwin, P. (2018). Jupiter's auroral-related stratospheric heating and chemistry II: Analysis of IRTF-TEXES spectra measured in December 2014. *Icarus*, *300*, 305 - 326. Retrieved from `http://www.sciencedirect.com/science/article/pii/S0019103517302154` doi: https://doi.org/10.1016/j.icarus.2017.09.016

A Additional Oxygen Tables

Table A.1. Altitude integrated ion production [cm^{-2} s^{-1}] from charge exchange collisions (i.e. TI, SC, SC+SS) for oxygen with incident ion energies between 10 and 25000 keV/u with no opacity effects considered. Everything has been normalized to a single incident ion/cm^2/s.

Ion Charge State	Energy 10 keV/u	50	75	100	200	300
O	2.27E+02	7.67E+02	8.12E+02	8.21E+02	8.26E+02	8.24E+02
O^{+}	1.34E+02	9.43E+02	1.16E+03	1.24E+03	1.28E+03	1.27E+03
O^{++}	1.25E+01	2.24E+02	3.99E+02	5.54E+02	7.11E+02	7.12E+02
O^{3+}	3.57E-01	2.73E+01	8.23E+01	1.78E+02	4.79E+02	5.03E+02
O^{4+}	3.06E-03	1.28E+00	7.01E+00	2.65E+01	2.67E+02	3.66E+02
O^{5+}	———-	4.16E-02	4.18E-01	2.90E+00	1.55E+02	4.79E+02
O^{6+}	———-	———-	1.04E-04	2.08E-03	1.33E+00	1.79E+01
O^{7+}	———-	———-	———-	1.04E-04	9.14E-02	2.33E+00

Ion Charge State	Energy 500 keV/u	1000	2000	5000	10000	25000
O	8.24E+02	8.23E+02	8.22E+02	8.22E+02	8.21E+02	8.28E+02
O^{+}	1.27E+03	1.27E+03	1.27E+03	1.27E+03	1.27E+03	1.28E+03
O^{++}	1.25E+01	2.24E+02	3.99E+02	5.54E+02	7.11E+02	7.12E+02
O^{3+}	5.03E+02	5.02E+02	5.03E+02	5.02E+02	5.01E+02	5.05E+02
O^{4+}	3.75E+02	3.74E+02	3.74E+02	3.74E+02	3.73E+02	3.77E+02
O^{5+}	6.73E+02	7.00E+02	7.00E+02	6.99E+02	6.98E+02	7.04E+02
O^{6+}	7.01E+01	1.17E+02	1.19E+02	1.19E+02	1.18E+02	1.19E+02
O^{7+}	2.35E+01	1.10E+02	1.49E+02	1.61E+02	1.63E+02	1.64E+02

Table A.2. Altitude integrated ion production [cm^{-2} s^{-1}] from direct excitation collisions (i.e. SI+SPEX, DI+SPEX, TEX+SPEX) for oxygen with incident ion energies between 10 and 25000 keV/u with no opacity effects considered. Everything has been normalized to a single incident ion/cm^2/s.

Ion Charge State	Energy 10 keV/u	50	75	100	200	300
O	2.53E+02	1.02E+03	1.13E+03	1.17E+03	1.18E+03	1.18E+03
O^{+}	1.94E+01	3.48E+02	5.33E+02	6.30E+02	6.86E+02	6.86E+02
O^{++}	3.21E+00	8.89E+01	1.95E+02	3.23E+02	5.17E+02	5.21E+02
O^{3+}	7.55E-02	7.28E+00	2.91E+01	8.40E+01	3.72E+02	4.10E+02
O^{4+}	7.14E-04	3.04E-01	1.67E+00	8.88E+00	1.43E+02	2.25E+02
O^{5+}	———	5.31E-03	9.45E-02	1.04E+00	1.15E+02	4.43E+02
O^{6+}	———	———	1.04E-04	2.29E-03	1.63E+00	1.97E+01
O^{7+}	———	———	———	———	1.59E-02	9.38E-01

Ion Charge State	Energy 500 keV/u	1000	2000	5000	10000	25000
O	1.18E+03	1.18E+03	1.18E+03	1.18E+03	1.17E+03	1.18E+03
O^{+}	6.85E+02	6.84E+02	6.83E+02	6.85E+02	6.83E+02	6.89E+02
O^{++}	5.21E+02	5.20E+02	5.20E+02	5.20E+02	5.19E+02	5.23E+02
O^{3+}	4.11E+02	4.10E+02	4.10E+02	4.10E+02	4.09E+02	4.13E+02
O^{4+}	2.39E+02	2.38E+02	2.38E+02	2.38E+02	2.38E+02	2.40E+02
O^{5+}	6.60E+02	6.91E+02	6.91E+02	6.90E+02	6.89E+02	6.96E+02
O^{6+}	7.00E+01	1.09E+02	1.11E+02	1.11E+02	1.11E+02	1.12E+02
O^{7+}	1.47E+01	9.39E+01	1.34E+02	1.48E+02	1.49E+02	1.51E+02

Table A.3. The X-ray efficiency ($[\mathrm{cm}^2\mathrm{sec}]^{-1}[\mathrm{keV/u}]^{-1}$) of outgoing photons as a function of initial ion energy including opacity effects. No opacity effects and the viewing angles of 0°, 80°, and 90° are displayed for atmosphere 1. The efficiency shown here is that solely from charge exchange collisions for oxygen. We also include the X-ray efficiencies that correspond to the JEDI energy bins at the time of writing.

Atmosphere 1 (Original atmosphere)

Energy	No Opacity		0°		80°		90°	
[keV/u]	O^{6+}	O^{7+}	O^{6+}	O^{7+}	O^{6+}	O^{7+}	O^{6+}	O^{7+}
100	0.00002	——-	0.00002	——-	0.00002	——-	0.00002	——-
121	0.00013	——-	0.00013	——-	0.00013	——-	0.00013	——-
125	0.00017	0.00001	0.00017	0.00001	0.00017	0.00001	0.00017	0.00001
150	0.00084	0.00004	0.00084	0.00004	0.00084	0.00004	0.00083	0.00004
175	0.00281	0.00017	0.00280	0.00017	0.00280	0.00017	0.00279	0.00017
200	0.00676	0.00045	0.00676	0.00045	0.00675	0.00045	0.00670	0.00045
218	0.01122	0.00083	0.01121	0.00083	0.01120	0.00083	0.01110	0.00082
250	0.02283	0.00201	0.02282	0.00201	0.02278	0.00201	0.02251	0.00199
300	0.04796	0.00569	0.04793	0.00569	0.04780	0.00567	0.04690	0.00560
350	0.07630	0.01209	0.07623	0.01208	0.07591	0.01204	0.07364	0.01182
400	0.10308	0.02163	0.10294	0.02161	0.10232	0.02151	0.09755	0.02098
450	0.12439	0.03339	0.12417	0.03335	0.12311	0.03316	0.11448	0.03205
456	0.12697	0.03509	0.12673	0.03504	0.12560	0.03483	0.11634	0.03363
500	0.13987	0.04676	0.13952	0.04668	0.13787	0.04634	0.12372	0.04429
600	0.15391	0.07349	0.15318	0.07328	0.14981	0.07241	0.11957	0.06671
700	0.15051	0.09296	0.14925	0.09254	0.14353	0.09083	0.09536	0.07866
800	0.14038	0.10470	0.13850	0.10395	0.13006	0.10107	0.06782	0.07982
900	0.12843	0.10958	0.12589	0.10844	0.11476	0.10415	0.04539	0.07304
1000	0.11703	0.11002	0.11385	0.10843	0.10024	0.10258	0.03000	0.06267
1250	0.09460	0.10269	0.08997	0.09985	0.07150	0.09008	0.01143	0.03800
1500	0.07939	0.09270	0.07349	0.08865	0.05176	0.07529	0.00491	0.02157
1750	0.06784	0.08262	0.06095	0.07756	0.03774	0.06155	0.00251	0.01233
2000	0.05952	0.07455	0.05169	0.06854	0.02774	0.05030	0.00138	0.00715
5000	0.02374	0.03229	0.01087	0.02029	0.00113	0.00440	0.00004	0.00018
10000	0.01182	0.01628	0.00121	0.00373	0.00007	0.00026	——-	0.00001
25000	0.00477	0.00657	0.00003	0.00009	——-	0.00001	——-	——-

Table A.4. The X-ray efficiency ($[\mathrm{cm}^2\mathrm{sec}]^{-1}[\mathrm{keV/u}]^{-1}$) of outgoing photons as a function of initial ion energy including opacity effects. No opacity effects and the viewing angles of 0°, 80°, and 90° are displayed for atmosphere 2. The efficiency shown here is that solely from charge exchange collisions for oxygen. We also include the X-ray efficiencies that correspond to the JEDI energy bins at the time of writing.

Atmosphere 2 (Well-mixed atmosphere)

Energy	No Opacity		0°		80°		90°	
[keV/u]	O^{6+}	O^{7+}	O^{6+}	O^{7+}	O^{6+}	O^{7+}	O^{6+}	O^{7+}
100	0.00002	—	0.00002	—	0.00002	—	0.00002	—
121	0.00013	—	0.00013	—	0.00013	—	0.00013	—
125	0.00017	0.00001	0.00017	0.00001	0.00017	0.00001	0.00017	0.00001
150	0.00084	0.00004	0.00084	0.00004	0.00083	0.00004	0.00081	0.00004
175	0.00281	0.00017	0.00280	0.00017	0.00279	0.00017	0.00270	0.00017
200	0.00676	0.00045	0.00675	0.00045	0.00670	0.00045	0.00646	0.00044
218	0.01122	0.00083	0.01120	0.00083	0.01112	0.00082	0.01065	0.00080
250	0.02283	0.00201	0.02278	0.00201	0.02257	0.00200	0.02135	0.00193
300	0.04796	0.00569	0.04783	0.00568	0.04719	0.00563	0.04346	0.00536
350	0.07630	0.01209	0.07601	0.01206	0.07462	0.01192	0.06620	0.01119
400	0.10308	0.02163	0.10255	0.02156	0.10008	0.02125	0.08452	0.01957
450	0.12439	0.03339	0.12357	0.03326	0.11976	0.03267	0.09518	0.02940
456	0.12697	0.03509	0.12610	0.03494	0.12210	0.03431	0.09618	0.03079
500	0.13987	0.04676	0.13871	0.04653	0.13337	0.04554	0.09835	0.03988
600	0.15391	0.07349	0.15199	0.07296	0.14328	0.07076	0.08631	0.05738
700	0.15051	0.09296	0.14783	0.09204	0.13597	0.08829	0.06296	0.06434
800	0.14038	0.10470	0.13701	0.10330	0.12234	0.09779	0.04145	0.06216
900	0.12843	0.10958	0.12444	0.10768	0.10746	0.10042	0.02621	0.05453
1000	0.11703	0.11002	0.11248	0.10761	0.09361	0.09867	0.01673	0.04529
1250	0.09460	0.10269	0.08885	0.09904	0.06658	0.08638	0.00626	0.02641
1500	0.07939	0.09270	0.07256	0.08792	0.04817	0.07213	0.00270	0.01487
1750	0.06784	0.08262	0.06018	0.07692	0.03512	0.05895	0.00140	0.00850
2000	0.05952	0.07455	0.05103	0.06798	0.02581	0.04817	0.00077	0.00493
5000	0.02374	0.03229	0.01072	0.02013	0.00105	0.00423	0.00003	0.00012
10000	0.01182	0.01628	0.00119	0.00369	0.00007	0.00025	—	0.00001
25000	0.00477	0.00657	0.00003	0.00009	—	0.00001	—	—

Table A.5. The X-ray efficiency ($[\text{cm}^2\text{sec}]^{-1}[\text{keV/u}]^{-1}$) of outgoing photons as a function of initial ion energy including opacity effects. No opacity effects and the viewing angles of 0°, 80°, and 90° are displayed for atmosphere 1. The efficiency shown here is that solely from direct excitation collisions for oxygen.

Atmosphere 1 (Original atmosphere)

Energy	No Opacity		0°		80°		90°	
[keV/u]	O^{6+}	O^{7+}	O^{6+}	O^{7+}	O^{6+}	O^{7+}	O^{6+}	O^{7+}
100	0.00003	—	0.00003	—	0.00003	—	0.00003	—
121	0.00014	—	0.00014	—	0.00014	—		
125	0.00020	—	0.00020	—	0.00020	—	0.00020	—
150	0.00098	—	0.00098	—	0.00098	—	0.00097	—
175	0.00313	0.00002	0.00313	0.00002	0.00313	0.00002	0.00311	0.00002
200	0.00747	0.00007	0.00746	0.00007	0.00745	0.00007	0.00740	0.00007
218	0.01242	0.00017	0.01242	0.00017	0.01240	0.00017	0.01230	0.00017
250	0.02443	0.00054	0.02442	0.00054	0.02437	0.00054	0.02408	0.00054
300	0.04852	0.00194	0.04849	0.00194	0.04835	0.00193	0.04741	0.00192
350	0.07465	0.00498	0.07458	0.00498	0.07426	0.00497	0.07195	0.00492
400	0.09801	0.01013	0.09788	0.01012	0.09726	0.01010	0.09252	0.00994
450	0.11545	0.01736	0.11523	0.01735	0.11421	0.01729	0.10580	0.01690
456	0.11761	0.01849	0.11738	0.01848	0.11629	0.01842	0.10727	0.01798
500	0.12752	0.02654	0.12719	0.02652	0.12562	0.02641	0.11202	0.02556
600	0.13589	0.04735	0.13522	0.04728	0.13209	0.04696	0.10395	0.04400
700	0.13063	0.06541	0.12949	0.06525	0.12430	0.06448	0.08060	0.05705
800	0.12044	0.07738	0.11876	0.07706	0.11125	0.07557	0.05622	0.06109
900	0.10968	0.08317	0.10744	0.08263	0.09765	0.08012	0.03734	0.05722
1000	0.09991	0.08502	0.09713	0.08419	0.08527	0.08044	0.02481	0.04944
1250	0.08049	0.08112	0.07653	0.07945	0.06070	0.07217	0.00968	0.02952
1500	0.06746	0.07423	0.06245	0.07164	0.04397	0.06090	0.00434	0.01657
1750	0.05762	0.06658	0.05179	0.06316	0.03211	0.04975	0.00233	0.00939
2000	0.05053	0.06048	0.04391	0.05623	0.02363	0.04057	0.00138	0.00550
5000	0.02016	0.02673	0.00932	0.01641	0.00104	0.00311	0.00015	0.00025
10000	0.01006	0.01347	0.00107	0.00266	0.00012	0.00022	0.00006	0.00007
25000	0.00406	0.00544	0.00005	0.00009	0.00003	0.00003	0.00003	0.00003

Table A.6. The X-ray efficiency ($[\mathrm{cm}^2\mathrm{sec}]^{-1}[\mathrm{keV/u}]^{-1}$) of outgoing photons as a function of initial ion energy including opacity effects. No opacity effects and the viewing angles of 0°, 80°, and 90° are displayed for atmosphere 2. The efficiency shown here is that solely from direct excitation collisions for oxygen.

Atmosphere 2 (Well-mixed atmosphere)

Energy	No Opacity		0°		80°		90°	
[keV/u]	O^{6+}	O^{7+}	O^{6+}	O^{7+}	O^{6+}	O^{7+}	O^{6+}	O^{7+}
100	0.00003	——-	0.00003	——-	0.00003	——-	0.00003	——-
121	0.00014	——-	0.00014	——-	0.00014	——-	0.00013	——-
125	0.00020	——-	0.00020	——-	0.00020	——-	0.00019	——-
150	0.00098	——-	0.00098	——-	0.00097	——-	0.00095	——-
175	0.00313	0.00002	0.00313	0.00002	0.00311	0.00002	0.00302	0.00002
200	0.00747	0.00007	0.00745	0.00007	0.00741	0.00007	0.00714	0.00007
218	0.01242	0.00017	0.01240	0.00017	0.01231	0.00017	0.01179	0.00017
250	0.02443	0.00054	0.02438	0.00054	0.02414	0.00054	0.02280	0.00053
300	0.04852	0.00194	0.04838	0.00193	0.04772	0.00192	0.04382	0.00185
350	0.07465	0.00498	0.07435	0.00497	0.07297	0.00493	0.06447	0.00469
400	0.09801	0.01013	0.09749	0.01010	0.09508	0.01000	0.07979	0.00933
450	0.11545	0.01736	0.11466	0.01731	0.11103	0.01708	0.08743	0.01561
456	0.11761	0.01849	0.11678	0.01844	0.11297	0.01819	0.08812	0.01656
500	0.12752	0.02654	0.12643	0.02645	0.12143	0.02603	0.08837	0.02315
600	0.13589	0.04735	0.13414	0.04711	0.12623	0.04602	0.07426	0.03805
700	0.13063	0.06541	0.12825	0.06495	0.11769	0.06282	0.05266	0.04678
800	0.12044	0.07738	0.11749	0.07664	0.10464	0.07322	0.03415	0.04740
900	0.10968	0.08317	0.10621	0.08210	0.09147	0.07727	0.02157	0.04220
1000	0.09991	0.08502	0.09598	0.08361	0.07968	0.07730	0.01396	0.03501
1250	0.08049	0.08112	0.07559	0.07883	0.05658	0.06902	0.00546	0.01989
1500	0.06746	0.07423	0.06167	0.07105	0.04095	0.05812	0.00254	0.01105
1750	0.05762	0.06658	0.05114	0.06264	0.02990	0.04744	0.00142	0.00628
2000	0.05053	0.06048	0.04336	0.05576	0.02200	0.03866	0.00088	0.00369
5000	0.02016	0.02673	0.00919	0.01626	0.00098	0.00297	0.00013	0.00021
10000	0.01006	0.01347	0.00106	0.00264	0.00012	0.00022	0.00006	0.00006
25000	0.00406	0.00544	0.00005	0.00008	0.00003	0.00003	0.00003	0.00003

B Additional Sulfur Tables

Table B.1. Altitude integrated ion production [cm^{-2} s^{-1}] from charge exchange collisions (i.e. TI, SC, SC+SS) for sulfur with incident ion energies between 10 and 2000 keV/u with no opacity effects considered. Everything has been normalized to a single incident ion/cm^2/s.

Ion Charge State	Energy 10 keV/u	50	75	100	200
S	2.33E+02	9.94E+02	1.07E+03	1.08E+03	1.08E+03
S^{+}	2.07E+02	2.24E+03	2.66E+03	2.78E+03	2.81E+03
S^{++}	3.88E+01	9.92E+02	1.51E+03	1.85E+03	2.09E+03
S^{3+}	2.16E+00	1.79E+02	4.61E+02	8.23E+02	1.42E+03
S^{4+}	3.01E-02	1.39E+01	6.23E+01	1.79E+02	8.22E+02
S^{5+}	3.57E-04	7.27E-01	5.21E+00	2.77E+01	6.14E+02
S^{6+}	——-	1.89E-03	3.04E-02	3.29E-01	4.12E+01
S^{7+}	——-	1.02E-04	6.12E-04	1.00E-02	4.99E+00
S^{8+}	——-	——-	——-	1.53E-04	3.35E-01
S^{9+}	——-	——-	——-	——-	2.23E-02
S^{10+}	——-	——-	——-	——-	7.14E-04
S^{11+}	——-	——-	——-	——-	5.10E-05
S^{12+}	——-	——-	——-	——-	——-
S^{13+}	——-	——-	——-	——-	——-
S^{14+}	——-	——-	——-	——-	——-
S^{15+}	——-	——-	——-	——-	——-

Ion Charge State	Energy 300 keV/u	500	1000	2000
S	1.08E+03	1.08E+03	1.08E+03	1.08E+03
S^{+}	2.81E+03	2.81E+03	2.81E+03	2.81E+03
S^{++}	2.09E+03	2.09E+03	2.09E+03	2.09E+03
S^{3+}	1.45E+03	1.45E+03	1.45E+03	1.45E+03
S^{4+}	9.50E+02	9.56E+02	9.56E+02	9.56E+02
S^{5+}	1.18E+03	1.33E+03	1.33E+03	1.33E+03
S^{6+}	1.87E+02	3.28E+02	3.29E+02	3.30E+02
S^{7+}	5.56E+01	1.86E+02	1.92E+02	1.92E+02
S^{8+}	1.03E+01	9.98E+01	1.16E+02	1.16E+02
S^{9+}	1.87E+00	6.18E+01	8.92E+01	8.92E+01
S^{10+}	2.31E-01	2.60E+01	5.34E+01	5.34E+01
S^{11+}	3.42E-02	1.66E+01	6.12E+01	6.13E+01
S^{12+}	7.96E-03	1.11E+01	7.91E+01	8.15E+01
S^{13+}	1.12E-03	1.03E+01	2.27E+02	2.78E+02
S^{14+}	——-	7.41E-02	1.19E+01	3.81E+01
S^{15+}	——-	4.14E-02	6.96E+00	2.39E+01

Table B.2. Altitude integrated ion production [cm^{-2} s^{-1}] from direct excitation collisions (i.e. SI+SPEX, DI+SPEX, TEX+SPEX) for sulfur with incident ion energies between 10 and 2000 keV/u with no opacity effects considered. Everything has been normalized to a single incident ion/cm^2/s.

Ion Charge State	Energy 10 keV/u	50	75	100	200
S	3.33E+02	2.58E+03	2.95E+03	3.05E+03	3.08E+03
S^{+}	4.71E+01	1.22E+03	1.72E+03	1.98E+03	2.12E+03
S^{++}	2.07E+00	1.78E+02	4.77E+02	7.89E+02	1.15E+03
S^{3+}	1.57E-01	3.13E+01	1.50E+02	3.73E+02	1.01E+03
S^{4+}	2.26E-03	2.27E+00	1.34E+01	6.17E+01	7.08E+02
S^{5+}	——-	1.07E-01	1.52E+00	1.20E+01	5.16E+02
S^{6+}	——-	1.51E-04	3.92E-03	7.59E-02	1.50E+01
S^{7+}	——-	——-	——-	6.53E-04	9.02E-01
S^{8+}	——-	——-	——-	——-	1.16E-01
S^{9+}	——-	——-	——-	——-	4.12E-03
S^{10+}	——-	——-	——-	——-	5.02E-04
S^{11+}	——-	——-	——-	——-	5.02E-05
S^{12+}	——-	——-	——-	——-	——-
S^{13+}	——-	——-	——-	——-	——-
S^{14+}	——-	——-	——-	——-	——-
S^{15+}	——-	——-	——-	——-	——-

Ion Charge State	Energy 300 keV/u	500	1000	2000
S	3.08E+03	3.07E+03	3.08E+03	3.08E+03
S^{+}	2.12E+03	2.12E+03	2.12E+03	2.12E+03
S^{++}	1.16E+03	1.16E+03	1.16E+03	1.16E+03
S^{3+}	1.08E+03	1.08E+03	1.08E+03	1.08E+03
S^{4+}	9.24E+02	9.41E+02	9.41E+02	9.42E+02
S^{5+}	1.20E+03	1.42E+03	1.42E+03	1.42E+03
S^{6+}	9.54E+01	2.01E+02	2.03E+02	2.03E+02
S^{7+}	1.72E+01	9.47E+01	1.00E+02	1.00E+02
S^{8+}	5.32E+00	6.71E+01	7.97E+01	7.96E+01
S^{9+}	6.79E-01	3.37E+01	5.15E+01	5.15E+01
S^{10+}	8.24E-02	1.65E+01	3.83E+01	3.80E+01
S^{11+}	1.30E-02	9.15E+00	3.52E+01	3.54E+01
S^{12+}	2.15E-03	6.59E+00	5.89E+01	6.06E+01
S^{13+}	6.50E-04	1.15E+01	2.46E+02	3.00E+02
S^{14+}	——-	1.25E-01	1.05E+01	2.97E+01
S^{15+}	——-	7.21E-02	2.08E+02	2.88E+03

Table B.3. The X-ray efficiency ($[cm^2 sec]^{-1}[keV/u]^{-1}$) of outgoing photons as a function of initial ion energy including opacity effects. No opacity effects and the viewing angle of 0° are displayed for atmosphere 1. The efficiency shown here is that solely from charge exchange collisions for sulfur.

Atmosphere 1 (Original atmosphere)

Energy	No Opacity						
[keV/u]	S^{8+}	S^{9+}	S^{10+}	S^{11+}	S^{12+}	S^{13+}	S^{14+}
125	0.00002	——-	——-	——-	——-	——-	——-
150	0.00010	——-	——-	——-	——-	——-	——-
175	0.00048	0.00002	——-	——-	——-	——-	——-
200	0.00168	0.00011	——-	——-	——-	——-	——-
250	0.01033	0.00119	0.00009	0.00001	——-	——-	——-
300	0.03435	0.00622	0.00077	0.00011	0.00003	——-	——-
350	0.07751	0.02099	0.00377	0.00086	0.00026	0.00007	——-
400	0.13211	0.05073	0.01291	0.00427	0.00181	0.00076	——-
450	0.17796	0.09057	0.03048	0.01437	0.00774	0.00495	0.00002
500	0.19957	0.12365	0.05208	0.03326	0.02226	0.02065	0.00015
600	0.19061	0.14001	0.07467	0.06741	0.06023	0.08874	0.00122
700	0.16565	0.12694	0.07368	0.07715	0.08247	0.15869	0.00334
800	0.14505	0.11168	0.06641	0.07405	0.08766	0.20345	0.00609
900	0.12878	0.09920	0.05931	0.06757	0.08488	0.22342	0.00907
1000	0.11593	0.08921	0.05339	0.06117	0.07910	0.22688	0.01191
1250	0.09275	0.07149	0.04272	0.04902	0.06474	0.20672	0.01681
1500	0.07726	0.05951	0.03565	0.04084	0.05431	0.18070	0.01895
1750	0.06618	0.05094	0.03055	0.03507	0.04660	0.15759	0.01950
2000	0.05796	0.04462	0.02672	0.03063	0.04077	0.13882	0.01907
Energy	0°						
[keV/u]	S^{8+}	S^{9+}	S^{10+}	S^{11+}	S^{12+}	S^{13+}	S^{14+}
125	0.00002	——-	——-	——-	——-	——-	——-
150	0.00010	——-	——-	——-	——-	——-	——-
175	0.00047	0.00002	——-	——-	——-	——-	——-
200	0.00167	0.00011	——-	——-	——-	——-	——-
250	0.01024	0.00119	0.00009	0.00001	——-	——-	——-
300	0.03391	0.00619	0.00077	0.00011	0.00003	——-	——-
350	0.07618	0.02083	0.00375	0.00086	0.00026	0.00007	——-
400	0.12911	0.05025	0.01284	0.00426	0.00181	0.00075	——-
450	0.17269	0.08948	0.03027	0.01433	0.00773	0.00494	0.00002
500	0.19194	0.12176	0.05162	0.03314	0.02221	0.02061	0.00015
600	0.17921	0.13648	0.07358	0.06701	0.05998	0.08846	0.00121
700	0.15150	0.12194	0.07190	0.07635	0.08191	0.15785	0.00334
800	0.12849	0.10528	0.06388	0.07278	0.08666	0.20172	0.00607
900	0.11009	0.09141	0.05598	0.06572	0.08331	0.22044	0.00904
1000	0.09534	0.08011	0.04923	0.05867	0.07686	0.22232	0.01185
1250	0.06888	0.05982	0.03679	0.04496	0.06068	0.19741	0.01664
1500	0.05167	0.04624	0.02854	0.03564	0.04878	0.16689	0.01860
1750	0.03981	0.03672	0.02272	0.02910	0.04003	0.14030	0.01896
2000	0.03125	0.02976	0.01839	0.02411	0.03343	0.11879	0.01834

Table B.4. The X-ray efficiency ($[\mathrm{cm}^2\mathrm{sec}]^{-1}[\mathrm{keV/u}]^{-1}$) of outgoing photons as a function of initial ion energy including opacity effects. Viewing angles of 80° and 90° are displayed for atmosphere 1. The efficiency shown here is that solely from charge exchange collisions for sulfur.

Atmosphere 1 (Original atmosphere)

Energy	80°						
[keV/u]	S^{8+}	S^{9+}	S^{10+}	S^{11+}	S^{12+}	S^{13+}	S^{14+}
125	0.00002	—	—	—	—	—	—
150	0.00010	—	—	—	—	—	—
175	0.00046	0.00002	—	—	—	—	—
200	0.00162	0.00011	—	—	—	—	—
250	0.00984	0.00116	0.00009	0.00001	—	—	—
300	0.03200	0.00603	0.00076	0.00011	0.00003	—	—
350	0.07051	0.02013	0.00367	0.00085	0.00026	0.00007	—
400	0.11672	0.04811	0.01250	0.00421	0.00179	0.00075	—
450	0.15163	0.08471	0.02930	0.01413	0.00765	0.00490	0.00002
500	0.16248	0.11359	0.04957	0.03258	0.02194	0.02041	0.00015
600	0.13816	0.12174	0.06880	0.06515	0.05884	0.08713	0.00121
700	0.10425	0.10197	0.06436	0.07277	0.07931	0.15406	0.00331
800	0.07775	0.08107	0.05370	0.06721	0.08217	0.19411	0.00601
900	0.05797	0.06380	0.04334	0.05798	0.07651	0.20778	0.00890
1000	0.04345	0.05016	0.03452	0.04872	0.06752	0.20369	0.01161
1250	0.02220	0.02817	0.01954	0.03095	0.04572	0.16341	0.01597
1500	0.01231	0.01657	0.01152	0.02018	0.03088	0.12204	0.01739
1750	0.00735	0.01025	0.00715	0.01371	0.02135	0.09018	0.01724
2000	0.00466	0.00662	0.00459	0.00952	0.01510	0.06700	0.01618
Energy	90°						
[keV/u]	S^{8+}	S^{9+}	S^{10+}	S^{11+}	S^{12+}	S^{13+}	S^{14+}
125	0.00001	—	—	—	—	—	—
150	0.00009	—	—	—	—	—	—
175	0.00041	0.00002	—	—	—	—	—
200	0.00140	0.00010	—	—	—	—	—
250	0.00796	0.00105	0.00008	0.00001	—	—	—
300	0.02387	0.00519	0.00068	0.00011	0.00003	—	—
350	0.04837	0.01656	0.00324	0.00080	0.00025	0.00006	—
400	0.07273	0.03760	0.01071	0.00391	0.00170	0.00072	—
450	0.08421	0.06225	0.02418	0.01292	0.00718	0.00468	0.00002
500	0.07789	0.07701	0.03900	0.02926	0.02035	0.01935	0.00015
600	0.04480	0.06372	0.04579	0.05407	0.05178	0.07970	0.00118
700	0.02137	0.03639	0.03238	0.05213	0.06319	0.13267	0.00318
800	0.01059	0.01843	0.01833	0.03799	0.05554	0.15203	0.00566
900	0.00599	0.00957	0.00963	0.02374	0.04068	0.14184	0.00817
1000	0.00379	0.00562	0.00534	0.01387	0.02666	0.11634	0.01033
1250	0.00163	0.00220	0.00186	0.00432	0.00872	0.05583	0.01299
1500	0.00088	0.00113	0.00092	0.00196	0.00368	0.02668	0.01312
1750	0.00053	0.00066	0.00053	0.00110	0.00192	0.01381	0.01241
2000	0.00035	0.00043	0.00034	0.00068	0.00114	0.00763	0.01131

Table B.5. The X-ray efficiency ($[\mathrm{cm^2 sec}]^{-1}[\mathrm{keV/u}]^{-1}$) of outgoing photons as a function of initial ion energy including opacity effects. No opacity effects and the viewing angle of 0° are displayed for atmosphere 2. The efficiency shown here is that solely from charge exchange collisions for sulfur.

Atmosphere 2 (Well-mixed atmosphere)

Energy	No Opacity						
[keV/u]	S^{8+}	S^{9+}	S^{10+}	S^{11+}	S^{12+}	S^{13+}	S^{14+}
125	0.00002	–	–	–	–	–	–
150	0.00010	–	–	–	–	–	–
175	0.00048	0.00002	–	–	–	–	–
200	0.00168	0.00011	–	–	–	–	–
250	0.01033	0.00119	0.00009	0.00001	–	–	–
300	0.03435	0.00622	0.00077	0.00011	0.00003	–	–
350	0.07751	0.02099	0.00377	0.00086	0.00026	0.00007	–
400	0.13211	0.05073	0.01291	0.00427	0.00181	0.00076	–
450	0.17796	0.09057	0.03048	0.01437	0.00774	0.00495	0.00002
500	0.19957	0.12365	0.05208	0.03326	0.02226	0.02065	0.00015
600	0.19061	0.14001	0.07467	0.06741	0.06023	0.08874	0.00122
700	0.16565	0.12694	0.07368	0.07715	0.08247	0.15869	0.00334
800	0.14505	0.11168	0.06641	0.07405	0.08766	0.20345	0.00609
900	0.12878	0.09920	0.05931	0.06757	0.08488	0.22342	0.00907
1000	0.11593	0.08921	0.05339	0.06117	0.07910	0.22688	0.01191
1250	0.09275	0.07149	0.04272	0.04902	0.06474	0.20672	0.01681
1500	0.07726	0.05951	0.03565	0.04084	0.05431	0.18070	0.01895
1750	0.06618	0.05094	0.03055	0.03507	0.04660	0.15759	0.01950
2000	0.05796	0.04462	0.02672	0.03063	0.04077	0.13882	0.01907
Energy	0°						
[keV/u]	S^{8+}	S^{9+}	S^{10+}	S^{11+}	S^{12+}	S^{13+}	S^{14+}
125	0.00002	–	–	–	–	–	–
150	0.00010	–	–	–	–	–	–
175	0.00047	0.00002	–	–	–	–	–
200	0.00165	0.00011	–	–	–	–	–
250	0.01012	0.00118	0.00009	0.00001	–	–	–
300	0.03339	0.00613	0.00076	0.00011	0.00003	–	–
350	0.07476	0.02060	0.00371	0.00086	0.00026	0.00007	–
400	0.12624	0.04958	0.01268	0.00422	0.00180	0.00075	–
450	0.16819	0.08807	0.02984	0.01421	0.00768	0.00492	0.00002
500	0.18611	0.11951	0.05076	0.03283	0.02204	0.02050	0.00015
600	0.17222	0.13299	0.07182	0.06607	0.05935	0.08780	0.00121
700	0.14454	0.11795	0.06954	0.07481	0.08066	0.15619	0.00333
800	0.12201	0.10123	0.06124	0.07081	0.08486	0.19885	0.00604
900	0.10425	0.08755	0.05331	0.06354	0.08112	0.21643	0.00899
1000	0.09015	0.07658	0.04670	0.05649	0.07450	0.21748	0.01177
1250	0.06503	0.05707	0.03477	0.04311	0.05850	0.19203	0.01650
1500	0.04875	0.04409	0.02694	0.03414	0.04696	0.16200	0.01842
1750	0.03754	0.03500	0.02144	0.02786	0.03851	0.13607	0.01877
2000	0.02947	0.02836	0.01735	0.02308	0.03216	0.11517	0.01814

Table B.6. The X-ray efficiency ($[\mathrm{cm}^2\mathrm{sec}]^{-1}[\mathrm{keV/u}]^{-1}$) of outgoing photons as a function of initial ion energy including opacity effects. Viewing angles of 80° and 90° are displayed for atmosphere 2. The efficiency shown here is that solely from charge exchange collisions for sulfur.

Atmosphere 2 (Well-mixed atmosphere)

Energy	80°						
[keV/u]	S^{8+}	S^{9+}	S^{10+}	S^{11+}	S^{12+}	S^{13+}	S^{14+}
125	0.00002	——-	——-	——-	——-	——-	——-
150	0.00009	——-	——-	——-	——-	——-	——-
175	0.00044	0.00002	——-	——-	——-	——-	——-
200	0.00154	0.00011	——-	——-	——-	——-	——-
250	0.00922	0.00112	0.00008	0.00001	——-	——-	——-
300	0.02947	0.00572	0.00072	0.00011	0.00003	——-	——-
350	0.06386	0.01891	0.00347	0.00082	0.00025	0.00007	——-
400	0.10384	0.04470	0.01169	0.00404	0.00173	0.00073	——-
450	0.13230	0.07776	0.02711	0.01348	0.00738	0.00478	0.00002
500	0.13862	0.10275	0.04526	0.03089	0.02106	0.01984	0.00015
600	0.11235	0.10593	0.06038	0.06028	0.05546	0.08362	0.00119
700	0.08137	0.08516	0.05375	0.06509	0.07285	0.14540	0.00325
800	0.05905	0.06551	0.04272	0.05787	0.07320	0.17956	0.00587
900	0.04337	0.05047	0.03323	0.04827	0.06613	0.18824	0.00866
1000	0.03227	0.03926	0.02591	0.03964	0.05694	0.18111	0.01123
1250	0.01640	0.02188	0.01442	0.02471	0.03752	0.14143	0.01531
1500	0.00909	0.01286	0.00847	0.01609	0.02521	0.10477	0.01662
1750	0.00543	0.00796	0.00526	0.01096	0.01743	0.07731	0.01647
2000	0.00345	0.00514	0.00338	0.00764	0.01236	0.05754	0.01547
Energy	90°						
[keV/u]	S^{8+}	S^{9+}	S^{10+}	S^{11+}	S^{12+}	S^{13+}	S^{14+}
125	0.00001	——-	——-	——-	——-	——-	——-
150	0.00007	——-	——-	——-	——-	——-	——-
175	0.00034	0.00002	——-	——-	——-	——-	——-
200	0.00113	0.00009	——-	——-	——-	——-	——-
250	0.00609	0.00086	0.00007	0.00001	——-	——-	——-
300	0.01732	0.00410	0.00055	0.00009	0.00002	——-	——-
350	0.03359	0.01259	0.00249	0.00067	0.00022	0.00006	——-
400	0.04824	0.02752	0.00793	0.00320	0.00144	0.00064	——-
450	0.05301	0.04366	0.01719	0.01029	0.00597	0.00411	0.00002
500	0.04589	0.05121	0.02633	0.02257	0.01652	0.01678	0.00014
600	0.02259	0.03628	0.02626	0.03697	0.03823	0.06468	0.00111
700	0.00948	0.01756	0.01518	0.03026	0.04100	0.09898	0.00293
800	0.00450	0.00803	0.00724	0.01850	0.03111	0.10298	0.00510
900	0.00257	0.00410	0.00349	0.01006	0.01997	0.08746	0.00724
1000	0.00164	0.00244	0.00194	0.00542	0.01186	0.06631	0.00905
1250	0.00071	0.00097	0.00070	0.00168	0.00362	0.02883	0.01131
1500	0.00038	0.00050	0.00035	0.00078	0.00153	0.01334	0.01163
1750	0.00023	0.00029	0.00020	0.00044	0.00080	0.00680	0.01122
2000	0.00015	0.00019	0.00013	0.00028	0.00048	0.00373	0.01044

Table B.7. The X-ray efficiency ($[\mathrm{cm^2 sec}]^{-1}[\mathrm{keV/u}]^{-1}$) of outgoing photons as a function of initial ion energy including opacity effects. No opacity effects and the viewing angle of 0° are displayed for atmosphere 1. The efficiency shown here is that solely from direct excitation collisions for sulfur.

Atmosphere 1 (Original atmosphere)

Energy	No Opacity						
[keV/u]	S^{8+}	S^{9+}	S^{10+}	S^{11+}	S^{12+}	S^{13+}	S^{14+}
125	—	—	—	—	—	—	—
150	0.00003	—	—	—	—	—	—
175	0.00013	—	—	—	—	—	—
200	0.00060	0.00002	—	—	—	—	—
250	0.00455	0.00035	0.00003	—	—	—	—
300	0.01774	0.00231	0.00027	0.00004	0.00001	0.00001	—
350	0.04474	0.00900	0.00164	0.00039	0.00010	0.00008	—
400	0.08190	0.02446	0.00655	0.00210	0.00079	0.00081	—
450	0.11585	0.04698	0.01763	0.00764	0.00404	0.00548	—
500	0.13365	0.06738	0.03289	0.01821	0.01317	0.02286	—
600	0.13013	0.07984	0.05156	0.03814	0.04072	0.09703	—
700	0.11346	0.07309	0.05221	0.04407	0.05900	0.17309	—
800	0.09936	0.06444	0.04732	0.04241	0.06448	0.22100	0.00001
900	0.08822	0.05710	0.04235	0.03873	0.06317	0.24218	0.00001
1000	0.07929	0.05126	0.03798	0.03508	0.05871	0.24513	0.00001
1250	0.06358	0.04104	0.03041	0.02820	0.04796	0.22260	0.00001
1500	0.05286	0.03429	0.02530	0.02351	0.04016	0.19461	0.00002
1750	0.04544	0.02937	0.02172	0.02016	0.03447	0.16986	0.00002
2000	0.03967	0.02567	0.01898	0.01767	0.03015	0.14960	0.00002
Energy	0°						
[keV/u]	S^{8+}	S^{9+}	S^{10+}	S^{11+}	S^{12+}	S^{13+}	S^{14+}
125	—	—	—	—	—	—	—
150	0.00003	—	—	—	—	—	—
175	0.00013	—	—	—	—	—	—
200	0.00059	0.00002	—	—	—	—	—
250	0.00451	0.00035	0.00003	—	—	—	—
300	0.01753	0.00230	0.00027	0.00004	0.00001	0.00001	—
350	0.04404	0.00894	0.00163	0.00039	0.00010	0.00008	—
400	0.08018	0.02425	0.00651	0.00209	0.00079	0.00081	—
450	0.11267	0.04648	0.01751	0.00761	0.00404	0.00547	—
500	0.12890	0.06645	0.03262	0.01813	0.01314	0.02282	—
600	0.12277	0.07801	0.05083	0.03786	0.04054	0.09677	—
700	0.10418	0.07044	0.05097	0.04351	0.05857	0.17232	—
800	0.08836	0.06100	0.04553	0.04151	0.06369	0.21940	0.00001
900	0.07571	0.05290	0.03995	0.03742	0.06190	0.23937	0.00001
1000	0.06546	0.04635	0.03495	0.03332	0.05688	0.24074	0.00001
1250	0.04740	0.03475	0.02604	0.02534	0.04458	0.21312	0.00001
1500	0.03547	0.02711	0.02007	0.01987	0.03553	0.18011	0.00001
1750	0.02743	0.02166	0.01593	0.01601	0.02897	0.15135	0.00002
2000	0.02147	0.01760	0.01283	0.01314	0.02400	0.12789	0.00002

Table B.8. The X-ray efficiency ($[\mathrm{cm}^2\mathrm{sec}]^{-1}[\mathrm{keV/u}]^{-1}$) of outgoing photons as a function of initial ion energy including opacity effects. Viewing angles of 80° and 90° are displayed for atmosphere 1. The efficiency shown here is that solely from direct excitation collisions for sulfur.

Atmosphere 1 (Original atmosphere)

Energy	80°						
[keV/u]	S^{8+}	S^{9+}	S^{10+}	S^{11+}	S^{12+}	S^{13+}	S^{14+}
125	———	———	———	———	———	———	———
150	0.00003	———	———	———	———	———	———
175	0.00013	———	———	———	———	———	———
200	0.00058	0.00002	———	———	———	———	———
250	0.00435	0.00034	0.00003	———	———	———	———
300	0.01663	0.00225	0.00027	0.00004	0.00001	0.00001	———
350	0.04099	0.00867	0.00160	0.00039	0.00010	0.00008	———
400	0.07301	0.02332	0.00635	0.00206	0.00079	0.00080	———
450	0.09983	0.04424	0.01696	0.00748	0.00399	0.00544	———
500	0.11030	0.06238	0.03137	0.01776	0.01297	0.02265	———
600	0.09587	0.07025	0.04762	0.03657	0.03972	0.09554	———
700	0.07267	0.05965	0.04568	0.04103	0.05659	0.16875	———
800	0.05414	0.04776	0.03827	0.03764	0.06014	0.21207	0.00001
900	0.04034	0.03773	0.03083	0.03206	0.05643	0.22680	0.00001
1000	0.03017	0.02981	0.02433	0.02647	0.04928	0.22159	0.00001
1250	0.01547	0.01713	0.01358	0.01595	0.03228	0.17560	0.00001
1500	0.00859	0.01035	0.00794	0.00980	0.02095	0.12857	0.00001
1750	0.00523	0.00655	0.00491	0.00630	0.01393	0.09243	0.00001
2000	0.00338	0.00430	0.00317	0.00419	0.00944	0.06624	0.00001
Energy	90°						
[keV/u]	S^{8+}	S^{9+}	S^{10+}	S^{11+}	S^{12+}	S^{13+}	S^{14+}
125	———	———	———	———	———	———	———
150	0.00002	———	———	———	———	———	———
175	0.00012	———	———	———	———	———	———
200	0.00050	0.00002	———	———	———	———	———
250	0.00358	0.00031	0.00002	———	———	———	———
300	0.01267	0.00196	0.00024	0.00004	0.00001	0.00001	———
350	0.02877	0.00727	0.00141	0.00036	0.00009	0.00007	———
400	0.04675	0.01867	0.00546	0.00189	0.00074	0.00077	———
450	0.05721	0.03341	0.01411	0.00674	0.00373	0.00521	———
500	0.05483	0.04355	0.02498	0.01562	0.01200	0.02156	———
600	0.03238	0.03846	0.03223	0.02923	0.03473	0.08782	———
700	0.01558	0.02249	0.02341	0.02754	0.04456	0.14553	———
800	0.00787	0.01159	0.01337	0.01911	0.03965	0.16435	0.00001
900	0.00463	0.00614	0.00715	0.01129	0.02864	0.14966	0.00001
1000	0.00307	0.00371	0.00406	0.00634	0.01796	0.11821	0.00001
1250	0.00156	0.00164	0.00160	0.00214	0.00546	0.05164	0.00001
1500	0.00097	0.00097	0.00095	0.00112	0.00240	0.02350	0.00001
1750	0.00070	0.00067	0.00063	0.00074	0.00137	0.01180	0.00001
2000	0.00055	0.00050	0.00047	0.00055	0.00088	0.00649	0.00001

Table B.9. The X-ray efficiency ($[\mathrm{cm}^2\mathrm{sec}]^{-1}[\mathrm{keV/u}]^{-1}$) of outgoing photons as a function of initial ion energy including opacity effects. No opacity effects and the viewing angle of 0° are displayed for atmosphere 2. The efficiency shown here is that solely from direct excitation collisions for sulfur.

Atmosphere 2 (Well-mixed atmosphere)

Energy	No Opacity						
[keV/u]	S^{8+}	S^{9+}	S^{10+}	S^{11+}	S^{12+}	S^{13+}	S^{14+}
125	——-	——-	——-	——-	——-	——-	——-
150	0.00003	——-	——-	——-	——-	——-	——-
175	0.00013	——-	——-	——-	——-	——-	——-
200	0.00060	0.00002	——-	——-	——-	——-	——-
250	0.00455	0.00035	0.00003	——-	——-	——-	——-
300	0.01774	0.00231	0.00027	0.00004	0.00001	0.00001	——-
350	0.04474	0.00900	0.00164	0.00039	0.00010	0.00008	——-
400	0.08190	0.02446	0.00655	0.00210	0.00079	0.00081	——-
450	0.11585	0.04698	0.01763	0.00764	0.00404	0.00548	——-
500	0.13365	0.06738	0.03289	0.01821	0.01317	0.02286	——-
600	0.13013	0.07984	0.05156	0.03814	0.04072	0.09703	——-
700	0.11346	0.07309	0.05221	0.04407	0.05900	0.17309	——-
800	0.09936	0.06444	0.04732	0.04241	0.06448	0.22100	0.00001
900	0.08822	0.05710	0.04235	0.03873	0.06317	0.24218	0.00001
1000	0.07929	0.05126	0.03798	0.03508	0.05871	0.24513	0.00001
1250	0.06358	0.04104	0.03041	0.02820	0.04796	0.22260	0.00001
1500	0.05286	0.03429	0.02530	0.02351	0.04016	0.19461	0.00002
1750	0.04544	0.02937	0.02172	0.02016	0.03447	0.16986	0.00002
2000	0.03967	0.02567	0.01898	0.01767	0.03015	0.14960	0.00002
Energy	0°						
[keV/u]	S^{8+}	S^{9+}	S^{10+}	S^{11+}	S^{12+}	S^{13+}	S^{14+}
125	——-	——-	——-	——-	——-	——-	——-
150	0.00003	——-	——-	——-	——-	——-	——-
175	0.00013	——-	——-	——-	——-	——-	——-
200	0.00059	0.00002	——-	——-	——-	——-	——-
250	0.00446	0.00034	0.00003	——-	——-	——-	——-
300	0.01729	0.00228	0.00027	0.00004	0.00001	0.00001	——-
350	0.04327	0.00885	0.00161	0.00039	0.00010	0.00008	——-
400	0.07851	0.02398	0.00643	0.00208	0.00079	0.00080	——-
450	0.10991	0.04587	0.01727	0.00754	0.00401	0.00545	——-
500	0.12520	0.06542	0.03209	0.01792	0.01303	0.02270	——-
600	0.11818	0.07634	0.04964	0.03722	0.04008	0.09601	——-
700	0.09954	0.06848	0.04930	0.04246	0.05760	0.17038	——-
800	0.08401	0.05901	0.04362	0.04015	0.06224	0.21602	0.00001
900	0.07178	0.05101	0.03800	0.03592	0.06010	0.23461	0.00001
1000	0.06198	0.04462	0.03310	0.03181	0.05491	0.23493	0.00001
1250	0.04481	0.03340	0.02456	0.02407	0.04274	0.20662	0.00001
1500	0.03351	0.02604	0.01891	0.01884	0.03400	0.17416	0.00001
1750	0.02591	0.02080	0.01500	0.01517	0.02770	0.14617	0.00002
2000	0.02028	0.01690	0.01208	0.01245	0.02294	0.12343	0.00001

Table B.10. The X-ray efficiency ($[\mathrm{cm}^2\mathrm{sec}]^{-1}[\mathrm{keV/u}]^{-1}$) of outgoing photons as a function of initial ion energy including opacity effects. Viewing angles of 80° and 90° are displayed for atmosphere 2. The efficiency shown here is that solely from direct excitation collisions for sulfur.

Atmosphere 2 (Well-mixed atmosphere)

Energy	80°						
[keV/u]	S^{8+}	S^{9+}	S^{10+}	S^{11+}	S^{12+}	S^{13+}	S^{14+}
125	——-	——-	——-	——-	——-	——-	——-
150	0.00003	——-	——-	——-	——-	——-	——-
175	0.00012	——-	——-	——-	——-	——-	——-
200	0.00055	0.00002	——-	——-	——-	——-	——-
250	0.00409	0.00033	0.00003	——-	——-	——-	——-
300	0.01540	0.00215	0.00026	0.00004	0.00001	0.00001	——-
350	0.03736	0.00823	0.00151	0.00037	0.00009	0.00008	——-
400	0.06542	0.02194	0.00594	0.00197	0.00076	0.00078	——-
450	0.08778	0.04118	0.01573	0.00708	0.00384	0.00529	——-
500	0.09491	0.05733	0.02874	0.01666	0.01242	0.02197	——-
600	0.07866	0.06250	0.04193	0.03330	0.03726	0.09138	——-
700	0.05722	0.05122	0.03823	0.03585	0.05161	0.15840	——-
800	0.04149	0.03987	0.03044	0.03138	0.05297	0.19449	0.00001
900	0.03047	0.03094	0.02359	0.02560	0.04793	0.20287	0.00001
1000	0.02265	0.02424	0.01820	0.02051	0.04058	0.19366	0.00001
1250	0.01161	0.01385	0.01001	0.01203	0.02560	0.14807	0.00001
1500	0.00648	0.00838	0.00588	0.00736	0.01646	0.10687	0.00001
1750	0.00398	0.00532	0.00366	0.00475	0.01092	0.07632	0.00001
2000	0.00260	0.00351	0.00238	0.00317	0.00740	0.05453	0.00001
Energy	90°						
[keV/u]	S^{8+}	S^{9+}	S^{10+}	S^{11+}	S^{12+}	S^{13+}	S^{14+}
125	——-	——-	——-	——-	——-	——-	——-
150	0.00002	——-	——-	——-	——-	——-	——-
175	0.00010	——-	——-	——-	——-	——-	——-
200	0.00041	0.00002	——-	——-	——-	——-	——-
250	0.00278	0.00026	0.00002	——-	——-	——-	——-
300	0.00938	0.00160	0.00020	0.00003	0.00001	——-	——-
350	0.02037	0.00575	0.00109	0.00029	0.00008	0.00007	——-
400	0.03168	0.01429	0.00409	0.00150	0.00063	0.00068	——-
450	0.03694	0.02459	0.01017	0.00518	0.00306	0.00452	——-
500	0.03333	0.03053	0.01721	0.01155	0.00963	0.01838	——-
600	0.01713	0.02370	0.01902	0.01879	0.02510	0.06918	——-
700	0.00752	0.01209	0.01157	0.01476	0.02803	0.10348	——-
800	0.00386	0.00581	0.00583	0.00853	0.02127	0.10372	0.00001
900	0.00240	0.00313	0.00308	0.00447	0.01331	0.08419	0.00001
1000	0.00168	0.00199	0.00184	0.00243	0.00747	0.06045	0.00001
1250	0.00096	0.00099	0.00086	0.00098	0.00226	0.02403	0.00001
1500	0.00066	0.00064	0.00058	0.00060	0.00108	0.01076	0.00001
1750	0.00051	0.00047	0.00042	0.00045	0.00068	0.00539	0.00001
2000	0.00042	0.00037	0.00033	0.00037	0.00047	0.00302	0.00001

C Discussion on Data Usage

In the appendix we have provided as much of the derived data as possible (the oxygen collision data made violable by Schultz et al. (2019)) with the goal that anyone can use it to estimate their own X-ray flux as long as they have access to an initial JEDI spectrum. Here we want to layout as clearly as possible how to take an ion flux and produce an X-ray power.

1. The first, and arguably most difficult, part is converting the JEDI energy spectrogram into a usable ion flux. To be done accurately, this requires knowing the width of each energy bin on JEDI at the time of measurement. We have included the energy bin widths in Table C.1 that correspond to the data in Figure 4. It is likely the energies bins will be changed and resized, if they have not already.
2. Once the bin widths are known, one can convert the intensity from counts/steradian/cm^2/s/keV to counts/cm^2/sec by multiplying each flux intensity by 2π and the corresponding energy bin width. A second thing to consider is that the first three energy bins cannot distinguish between oxygen and sulfur ions. In this study we used an O:S ratio of 2:1 to separate the flux in the first three energy bins, motivated by the likely source of SO_2 from Io's volcanoes. A different ratio can be used, but those low energies will not affect X-ray production, anyway.
3. Once an intensity of counts/cm^2/s vs. ion energy (in keV/u, not total energy) is obtained, one can multiply the intensity by the ion energy (keV/u) and the X-ray efficiency for each charge state of the ion species at a given ion energy in Appendix A or B. To account for all X-rays, charge exchange and direct excitation need to be considered, in which case the X-ray efficiencies can be summed together. This will result in the number of photons/cm^2/s produced by each ion charge state and species.
4. Summing the photon production rate for each charge state together will give the total X-ray production rate for a given JEDI pass.
5. Multiplying the photon production rate by the average photon energy, 1.6x10^{-19} J/eV, 10^6 μW/W, and 10^4 cm^2/m^2 will yield the power in μW/m^2. In general, the average photon energy is likely between 500-600 eV. If sulfur emission is higher than oxygen, then 500 eV is more accurate and if oxygen emission is greater, the average photon energy probably tends closer to 600 eV.

As an example, for the JEDI oxygen measurement discussed in this text, the total photon production and power is calculated at each step in Table C.1.

The total X-ray production shown in Table C.1 is only about 7% percent higher than what is shown in Figure 12, where the power flux was found by integrating over every photon energy. This exact same process can be used for sulfur, but in this example sulfur emission is much less than oxygen.

Table C.1. Example of calculating X-ray production rates associated with JEDI oxygen ion flux measurements.

Oxygen				
Energy [keV]	JEDI Flux* [c/str/cm^2/s/keV]	Energy Bin Width [keV]	Intensity [c/cm^2/s]	Energy [keV/u]
171	249.9	66	103631	11
240	339.7	71	151542	15
324	279.0	105	184066	20
477	219.8	216	298306	30
746	89.50	346	194571	47
956	43.61	251	68776	60
1240	22.56	300	42525	78
1930	8.687	880	48032	121
3490	3.018	2280	43235	218
7300	0.914	5340	30667	456
Energy [keV/u]	X-Ray Efficiency† [cm^{2}sec]$^{-1}$[keV/u]$^{-1}$	X-ray Production photons/cm^2/s		
11	0.0000	0.000		
15	0.0000	0.000		
20	0.0000	0.000		
30	0.0000	0.000		
47	0.0000	0.000		
60	0.0000	0.000		
78	0.0000	0.000		
121	0.0003	1.74x10^3		
218	0.0246	2.32x10^5		
456	0.2951	4.13x10^6		
Total power flux [μW/m^2]:		4.2		

* These are the same flux measurements as those shown in Figure 4.
† X-ray efficiency values in Appendix A or B. These values are the sum of O^{6+} and O^{7+} from both charge exchange and direct excitation for an exit angle of 80° in atmosphere 1.